X-ray micro-tomographic imaging and modelling of saline ice properties in concrete frost salt scaling experiments

Maus, Sönke; Bahafid, Sara; Hendriks, Max; Jacobsen, Stefan; Geiker, Mette Rica

Important note
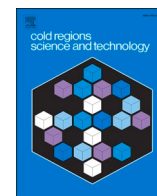To cite this publication, please use the final published version (if applicable).
Please check the document version above.

X-ray micro-tomographic imaging and modelling of saline ice properties in concrete frost salt scaling experiments

Sönke Maus [a,*], Sara Bahafid [b,c], Max Hendriks [b,d], Stefan Jacobsen [b], Mette Rica Geiker [b,e]

[a] Department of Civil and Environmental Engineering, Norwegian University of Science and Technology, 7491 Trondheim, Norway
[b] Department of Structural Engineering, Norwegian University of Science and Technology, 7491 Trondheim, Norway
[c] Holcim Innovation Center, 38070 Saint Quentin Fallavier, France
[d] Department of Engineering Structures, Delft University of Technology, Delft, The Netherlands
[e] PoreLab, Department of Physics, Norwegian University of Science and Technology, 7491 Trondheim, Norway

A B S T R A C T

Frost salt scaling of concrete is related to cyclic freezing and melting of a few millimeter thick deicer solution on the surface of the concrete. It is almost absent when pure water is freezing and reaches a maximum at a so-called pessimum concentration that for NaCl is around 3%. Different mechanisms have been suggested to explain this pessimum and frost salt scaling in general, ranging from the transport of moisture and growth of ice within the pore space of concrete ("cryogenic suction") to crack formation in the saline ice layer followed by spalling off the surface ("glue-spall"). Though in these theories the saline ice layer, that forms in concrete frost salt scaling experiments, plays a major role, so far little is known about its properties. We present a characterisation and an analysis of the microstructure of this saline ice layer by means of 3D X-ray microtomography. We found that the morphology of the saline ice is very similar to young, columnar sea ice, with lamellae of ice and brine oriented in the direction of freezing. On the basis of the microscopic 3D image data, we formulated percolation-based models of macroscopic properties (e.g., strength, thermal expansion coefficient, porosity metrics) relevant for different proposed frost salt scaling mechanisms. Model results and observations suggest that the ice growth velocity, direction and confinement, have a major impact on the pore structure of saline ice, thereby governing both mechanical and transport properties. These properties in turn are expected to affect proposed frost salt scaling mechanisms of concrete. The microstructure length scales in the ice-brine composite (lamellar spacing, pore width) are comparable to those for concrete (air void spacing and size), suggesting complex poro-mechanical interaction at the interface of concrete and saline ice. The results highlight the importance of studying saline ice properties to improve predictions of frost salt scaling processes.

1. Introduction

The freezing of saline solutions often results in porous ice media with multiple phases and a complex microstructure that determines their material properties. One prominent example is the formation of sea ice with strongly temperature-dependent properties that impact polar climate in many ways (e.g., Weeks, 2010). Examples from engineering fields are the properties of saline ice slurries in refrigeration applications, the de-icing of winter roads, and frost damage to structures. One of the frost damage types observed on concrete is known as *frost salt scaling*: cyclic freezing and thawing of water with deicers (salt, urea, alcohol) may result in surface damage of concrete elements and impact their durability.

Frost salt scaling at the surface of concrete, emerging in form of millimeter sized flakes (Brun et al., 2021), has been studied for more than half a century (Powers, 1954). The resistance of concrete to frost salt scaling depends on composition and production of the concrete (e.g, ASTM C457, EN206 and EN12390–9). It also depends on the nature of the freezing solution, being almost absent when the surface water layer is free of deicers. It has been frequently reported that the scaling is largest for freezing of saline solutions with intermediate concentrations of approximately 3% NaCl by mass, the so-called *pessimum effect*. A second aspect is the finding that air voids tend to prevent frost salt scaling. From a variety of damage mechanisms that have been suggested over time (e.g., Valenza and Scherer, 2007; Müller et al., 2019), two models appear most consistent with the effects of air voids and pessimal

---

* Corresponding author.
E-mail address: sonke.maus@ntnu.no (S. Maus).

salt concentration. The so called *cryogenic suction* mechanism, first suggested by Lindmark (1998) and extended by Liu and Hansen (2015), assumes that growth of micro-ice lenses causes damage of concrete. According to this hypothesis the freezing of the pore solution in concrete starts in capillary pores and grows into (micrometer sized) air voids, while the pore liquid in smaller (few nanometer sized) pores remains unfrozen. The unfrozen pore solution is then drawn towards the ice lenses. Here the pore solution freezes until thermodynamic equilibrium between the ice lenses and the surrounding pore solution is reached. This equilibrium is determined by the freezing point depression due to increased solute concentration and the size of the gel pores. The essence of the cryogenic suction theory is the consideration of brine in the external saline ice layer as an additional liquid source. The growth of surface-near ice lenses then causes scaling. The second approach proposed by Valenza and Scherer (2006) assumes that ice-concrete damage follows the same physical process as *glue spalling* (glass chipping) used for manufacturing ornamental glass (Gulati and Hagy, 1982). Due to this hypothesis the surface scaling is related to the fracture and mechanical action of the external saline ice layer. It is based on the assumption that stresses evolve due to the thermal mismatch during cooling and contraction of ice and concrete. In the ice-brine composite these stresses are supposed to initiate cracks upon exceeding the tensile strength of ice, that in turn propagate into the concrete and create damage. In a recent study (Bahafid et al., 2022) extended the work by Gulati and Hagy (1982) and studied stresses at the interface of saline ice and concrete by 2D numerical simulations. Their results suggest that the saline ice microstructure (pore and ice length scales) plays an important role for creating stress concentrations and maximum stresses at the interface. Similar to the saline ice failure stress considered by Valenza and Scherer (2006), also the interface (glue-spall) stress studied by Bahafid et al. (2022) depends essentially on the thermal expansion mismatch of saline ice and concrete. More recently, it has also been proposed that frost salt scaling may be related to brine expulsion from saline ice during freezing, creating pore pressure at the saline ice-concrete interface and subsequent up-lift of the ice-brine layer (Yener, 2015).

The proposed mechanisms thus differ fundamentally in the assumed process leading to frost salt scaling, ranging from crack propagation and stress concentration due to thermal expansion ("glue spall"), ice lens growth near the surface yet inside the concrete ("cryogenic suction") to pore pressure build up and adhesive failure between the saline ice and concrete ("brine expulsion"). However, the question of which model describes the frost salt scaling process most correctly, has remained unsolved. Plausible arguments for the existence of a salt pessimum have been proposed for all three mechanisms, yet so far no concise theory has been offered that quantitatively explains the pessimum concentration for frost salt scaling of concrete. In all model approaches, cryogenic suction, glue-spall and brine expulsion, an important role has been attributed to the properties and microstructure of the saline ice layer, yet observations of the saline ice microstructure in frost salt scaling experiments, and of its mechanical properties (e.g., elastic modulus, tensile strength), are absent. All approaches to estimate these properties of thin saline ice layers have been based on models and parametrisations developed for much thicker and older sea ice (Valenza and Scherer, 2006; Valenza and Scherer, 2007; Bahafid et al., 2022).

The primary objective of the present study has been to fill this observational gap of the microstructure of saline ice during frost salt scaling. Secondary objectives are to (i) investigate how salt concentration and growth velocity affect saline ice microstructure when frozen on a concrete surface in various ways, (ii) to relate mechanical (strength, elasticity and creep) and fluid transport properties (permeability and percolation of the pore space) of the saline ice to this microstructure and (iii) to investigate to what degree properties and models derived for sea ice are applicable to frost salt scaling. To achieve these objectives we performed non-destructive imaging by X-ray computed micro-tomography (micro-CT) which has become the method of choice to unravel the 3D microstructure and physics of porous media (Desrues

et al., 2006; Cnudde and Boone, 2013), and is also increasingly used to characterise the microstructure of concrete (Gallucci et al., 2007; Gopalakrishnan et al., 2007; Promentilla and Sugiyama, 2010; Brisard et al., 2020; Kong et al., 2020). Based on this 3D imagery we follow recent work on sea ice (Pringle et al., 2009; Maus et al., 2021) to derive percolation-based models of microscopic and bulk properties of thin saline ice layers. An important aspect of our approach is based on recent modelling of the cellular microstructure of sea ice: It has long been known that seawater, under most natural conditions, freezes with a lamellar interface, consisting of elongated vertical plates (Walker, 1859; Hamberg, 1895; Drygalski, 1897). These patterns can be explained by the linear stability theory for a planar interface formulated in 1964 (Mullins and Sekerka, 1964). The instability of the freezing interface is related to so-called "constitutional supercooling" that evolves at the freezing interface, where solute is released from almost pure ice crystals, due to the large difference between heat and solute diffusion. The theory has been shown to predict the spacing of ice lamellae in sea ice (as well for freezing NaCl solutions) over 5 orders of magnitude in the growth velocity (Maus, 2007; Maus, 2020).

The present work is structured as follows. In Section 2, after introducing the procedures of our frost salt scaling experiments, we define the relevant saline ice properties (bulk and microstructure: e.g., pore sizes, brine volume fraction, density, coefficient of thermal expansion, tensile strength), and how they can be obtained from solute concentration, temperature and microstructure information. We also describe the imaging technique (micro-CT) and equipment used. In the results section we present first 3D X-ray tomographic imagery of the microstructure of saline ice growing in a thin layer on the surface of concrete during frost salt scaling experiments, and quantitatively analyse the 3D pore space of the brine-ice composite grown from different solution salinities. We compare these results to recent findings on the freezing process, microstructure and properties of sea ice. Analogous to sea ice, the microstructure data are used to develop a percolation model of the pore space evolution (e.g., pore scales and connectivity), and to evaluate microstructure-based strength models for the strength of saline ice. In the discussion we extend the results in two ways. We (i) analyse the dependence of saline ice microstructure and properties on the ice growth velocity, and (ii) implement this dependence in the proposed models for percolation and microstructure evolution. This allows us to show how several properties relevant for frost salt scaling (pore sizes, strength and visco-elastic creep, coefficient of thermal expansion, pore pressure) depend on the brine volume fraction (and thus on ice temperature and solute concentration) and the growth velocity of saline ice. We close with some conclusions on how the results can be used in future studies of frost salt scaling.

2. Modelling and methods

2.1. Concrete specimen for frost salt scaling

An air-entrained concrete was mixed by the use of a counter-current rotating pan mixer Eirich at SINTEF concrete laboratory. The concrete mix contained 4 % of silica fume and 33 % of siliceous fly-ash by mass of binder. The water to binder ratio was 0.40. The detailed mixing procedure and characteristics of fresh and hardened concrete are given by Shpak (2020). After demoulding, the concrete block was cured under water for 2 years. Cores of 39 mm diameter were drilled out of the concrete block and sawn into discs of 1 cm thickness. To obtain non-leaking specimen during the freeze–thaw test first a non-absorptive marine glue was applied to the specimens' sides and bottom surface. The glued specimen surfaces were then wrapped in butyl tape to provide a tight non-absorptive dam above the concrete surface to be exposed to saline solution. The final specimens had a glue + butyl layer thickness of 2.3 ± 0.2 mm and a total diameter (butyl + concrete) of 43 to 44 mm. After wrapping, the specimens were pre-conditioned for 3 days by pouring a 3-mm-thick layer of demineralised water on the concrete

surface. Before the freezing of the specimen this preconditioning water was removed, and a saline solution (of thickness 3 to 13 mm) was poured on the specimen. Fig. 1 shows top and side views of the specimen for frost salt scaling experiments.

2.2. Saline ice growth experiments

Growth experiments of saline ice layers on the concrete discs have been performed in several ways, summarised in Table 1. The different settings were chosen to evaluate the microstructure for different growth modes and directions, solute concentrations and water layer thicknesses. Most experiments were done with NaCl concentrations in the range 10 to 120‰ by mass. Due to issues with image quality at low solute concentrations (contrast and resolution) to be discussed below we also performed experiments with CsCl solutions and mixtures of CsCl and NaCl. The concentration of CsCl and the mixtures were chosen to reflect the same freezing point depression as of NaCl. For the freezing experiments three growth modes, with experimental details shown in Fig. 1, were used. While ice growth is 3-dimensional in all settings, its primary direction is vertical in the direction of the cylindrical specimen axis, and these linear growth rates are estimated as follows:

I. *Constant cooling rate (1a to 6b)*. The frost salt scaling specimens (concrete with saline solution on top) were subjected to a controlled cooling rate (linear temperature change with time) in a Vötsch high-precision freeze–thaw chamber. The specimen were, with spacing 3–4 cm, placed in a $12 \times 12 \times 8$ cm (L $\times$ B $\times$ H) insulating box (20 mm thick styrofoam at the bottom and on the sides) that is normally used for frost salt scaling tests with larger specimen. The box was covered with a plastic film, as in a standard frost scaling slab test. However, the heat transfer was, in contrast to the standard slab test, taking through both the surface and the lateral surface of the cylindrical specimen. During the first three hours the temperature was lowered from 20 °C to −5 °C, followed by a further lowering to −20 °C over 9 h. The temperature was then maintained at −20 °C for an additional 4 h, followed by micro-CT imaging within the next 5 h.[1]

II. *Constant temperature, upward growth (1-up to 6-up)*. The specimens were laterally insulated by a styrofoam tube insulation of 1.5 cm thickness to minimize lateral heat loss, and from top with a 2 cm thick styrofoam lid. They were placed on a 1 cm thick aluminium plate at the bottom of a freezer (WAECO Coolfreeze T56, calibrated within 0.5 °C before the experiment) that was kept at constant temperature of −8 °C. The specimens, with initial temperature of 20 °C, were cooled for 24 h. Then the freezer temperature was set to −20 °C and the samples were equilibrated to this temperature for another 24 h, followed by micro-CT imaging.

III. *Constant temperature, downward growth (1-do to 6-do)*. For the downward growth the specimen were laterally insulated as in II, as well as insulated from the bottom by 5 cm thick styrofoam. No lid was used and the cooling was taking place due to direct air-solution contact. Cooling and freezing then proceeded in the same way as for II.

Unidirectional growth velocities at the onset of ice growth in the salt solution on the surface of the concrete are estimated for upward and downward growth as follows. The heat transfer through the bottom (upward growth, II) and free surface (downward growth, III) was determined by measuring the temperature change during the cooling phase of the saline solution. For the upward growth, with the sample bottom in contact with a 1-cm-thick aluminum plate, the results were consistent with conductive heat flow through the butyl-concrete bottom. For such a two-layer medium the effective thermal conductivity k_{cb} may be written as

$$k_{cb} = \frac{k_c k_b}{k_c h_b / H + k_b h_c / H}, \tag{1}$$

where k_c and k_b are the thermal conductivities of concrete ($\approx 2.0 W K^{-1} m^{-1}$ from Zehfuss et al. (2020)) and butyl rubber ($\approx 0.12 W K^{-1} m^{-1}$ from Thompson (1947)) and h_b / H and h_c / H their relative thickness ($h_c = 10$ mm, $h_b = 2$ mm, $H = h_c + h_b = 12$ mm). This gives an effective conductivity of $k_{cb} \approx 0.55$ WK^{-1}m^{-1}. The linear growth velocity is then estimated from

$$V = k_{cb} \frac{T_a - T_f}{H L_f \rho_i}, \tag{2}$$

where T_a is the temperature in the freezer (-8 °C), T_f the freezing temperature of the solution and L_f the latent heat of fusion (0.33 MJkg^{-3}). For a 30‰ NaCl saline solution with freezing point $T_f \approx −1.8$ °C this gives a growth velocity of 8.1 cm/day. For the 20‰ NaCl solution the growth in our experiments is slightly ($\approx 10\%$) larger.

For the downward growth (III) the growth rate is related to convective heat transfer at the air–water interface. Our estimate of $Q_T \approx 20 W m^{-2} K^{-1}$ obtained during the cooling phase likely includes some lateral heat loss due to imperfect insulation. It can be converted to a linear growth velocity

$$V = Q_T \frac{T_a - T_f}{L_f \rho_i}, \tag{3}$$

For a 30‰ NaCl saline solution with freezing point $T_f \approx −1.8$ °C this gives a growth velocity of 3.5 cm/day.

For the experiments with a linear temperature increase over time (I), the linear ice growth velocity is more difficult to estimate. The main heat loss is taking place laterally from the cylindrical specimen. Due to the larger height of the lower concrete part (10 mm + 0.2 mm butyl) compared to the solution (3 mm), the lower heat capacity yet larger thermal conductivity of concrete compared to water, we expect that freezing starts from the concrete-solution interface and proceeds upwards from there. The detailed heat flow is, however, of complicated three-dimensional nature. The onset of freezing is estimated on the basis of time-series of temperature in the air T_a and the solution T_s close to the concrete-solution interface shown in Fig. 2. These show the same behaviour as reported by other authors (e.g., Fagerlund, 1992) for concrete and air: the solution temperature is decreasing close to linearly but at a smaller rate than the air temperature. The point a which the solution temperature jumps by several degrees is associated with the onset of ice formation, leading to a strong drop in the supercooling, and a change from $T_s \approx −4.1$ °C to $T_s \approx −0.6$ °C (the freezing point for experiment 1b to which the timeseries refers). This happened at $T_a \approx −6.3$ °C which we also assume as the temperature at the outer surface of the concrete specimen at the onset of ice formation. We also assume that the average temperature at this stage drops back to the freezing point 0 °C and thus estimate the linear growth velocity from the temperature difference $(T_a − T_f) \approx −6.3$ °C using Eq. (2), which gives 8.2 cm/day. For the freezing run with a solution salinity of 30‰ almost the same temperature difference (6.2 °C) was observed (not shown). We thus use this estimate of the growth velocity for all solute concentrations (Table 1).

2.3. Saline ice properties

2.3.1. Salinity, density and brine porosity

While cooling below its freezing point, a saline solution of solute concentration S_0 freezes partially, creating a composite of almost pure ice crystals and concentrated brine ($S > S_0$) in thermodynamic equilibrium at the new temperature. For this dependence of freezing point T_f on solute concentration S of NaCl in water we use the relationship suggested by Maus (2007) based on the tabulated data from Zaytsev and

---

[1] The temperature–time history is in accordance with the freezing part of the EN 12390–9 cycle used for the slab test.
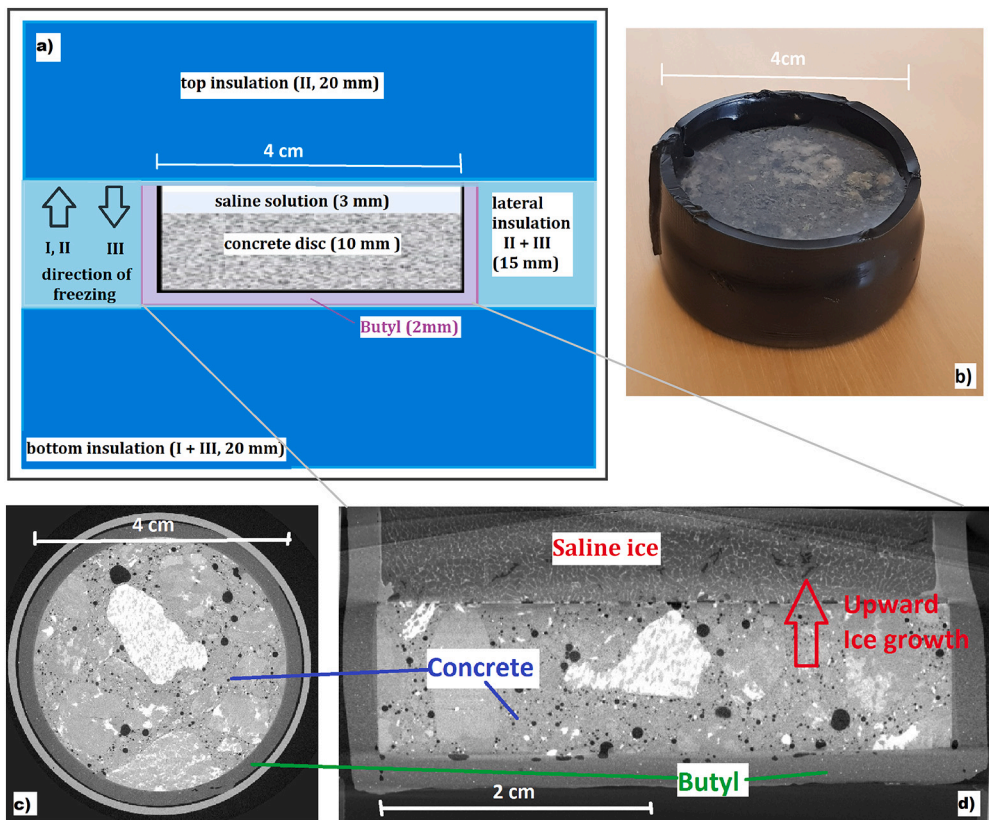
**Fig. 1.** Specimen used in frost salt scaling experiments: a) illustration of specimen embedding into styrofoam insulation for the three different ice growth methods and directions (I, II, III); b) photography of a specimen wrapped in butyl, with frozen saline solution at the surface; c) slice of concrete, wrapped in butyl, and inside a sample holder (top view, micro-CT based image); d) side view of the specimen with ice-brine composite (brine appearing brigh) on top, showing the butyl wrapping around; here the upward freezing direction (I, II) is indicated (micro-CT based image).

Table 1

Conditions of the freezing experiments of solutions (of thickness H_w) on concrete specimen for which X-ray tomographic images were obtained. Experiments were either performed with a constant temperature $T_{air} = -8\,°C$ in the freezing chamber, or with a linear cooling rate ($20 \rightarrow -20\,°C$). Freezing temperatures T_f of saline solutions containing both CsCl and NaCl are estimated from the sum of freezing point depressions. The growth modes (see text) are I: $\uparrow\rightarrow$ - primarily upward (constant cooling rate); II: $\uparrow$ - upward (constant temperature) and III: $\downarrow$ - downward (constant temperature). For estimation of growth velocities see the text.

Specimen Nr	NaCl ‰	CsCl ‰	T_f °C	T_{air} °C	H_w mm	Growth cm/day	Freezing method and direction
1a	0	0	0	20→ −20	3	8.2	I, ↑→
1b	10	0	−0.60	20→ −20	3	8.2	I, ↑→
2a	0	10	−0.21	20→ −20	3	8.2	I, ↑→
2b	30	0	−1.80	20→ −20	3	8.2	I, ↑→
3a	120	0	−8.21	20→ −20	3	8.2	I, ↑→
3b	30	0	−1.80	20→ −20	5	8.2	I, ↑→
4a	70	0	−4.39	20→ −20	3	8.2	I, ↑→
4b	120	0	−8.21	20→ −20	3	8.2	I, ↑→
5a	120	0	−8.21	20→ −20	3	8.2	I, ↑→
5b	30	0	−1.80	20→ −20	3	8.2	I, ↑→
6a	0	29	−0.60	20→ −20	3	8.2	I, ↑→
6b	0	87	−1.80	20→ −20	3	8.2	I, ↑→
1-up	20	0	−1.19	−8	8	8.9	II, ↑
2-up	30	0	−1.80	−8	5	8.1	II, ↑
3-up	18	6	−1.19	−8	6	8.9	II, ↑
4-up	27	9	−1.80	−8	6	8.1	II, ↑
5-up	15	15	−1.19	−8	6	8.9	II, ↑
6-up	20	20	−1.60	−8	7	8.3	II, ↑
1-do	20	0	−1.19	−8	11	3.9	III, ↓
2-do	30	0	−1.80	−8	12	3.5	III, ↓
3-do	18	6	−1.19	−8	10	3.9	III, ↓
4-do	27	9	−1.80	−8	13	3.5	III, ↓
5-do	15	15	−1.19	−8	13	3.9	III, ↓
6-do	20	20	−1.60	−8	13	3.6	III, ↓
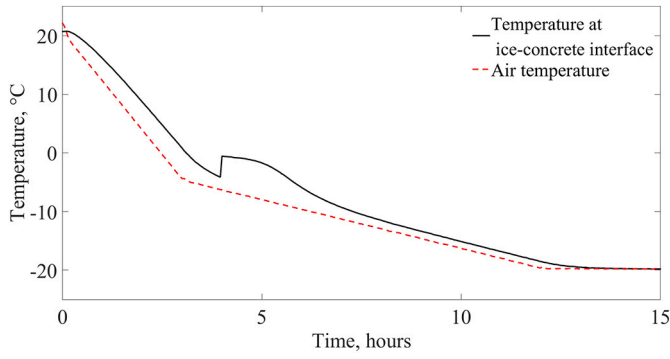
Fig. 2. Time series if temperature in air (cooling chamber) and at the saline ice-concrete interface for method I (experiment 1b). The temperature increase at the interface after approximately 4 h reflects the onset of freezing.

Aseyev (1992), see Appendix A. The solid ice volume fraction ϕ_s of the saline solution then increase by partial solidification of the solution's liquid fraction ϕ_b. In the absence of air $\phi_s = 1 - \phi_b$. Based on conservation of mass and salt

$$\phi_b = \left(1 + \left(\frac{S_b}{S_i} - 1\right)\frac{\rho_b}{\rho_i}\right)^{-1}, \tag{4}$$

where S_b and ρ_b are the brine salinity and density and ρ_i is the density of pure ice, also given in Appendix A.

The bulk density of saline ice is then obtained from

$$\rho_{si} = \phi_b\rho_b + (1 - \phi_b)\rho_i \tag{5}$$

which is again valid in the absence of gas. The coefficient α_{si} of thermal expansion of sea ice may then be computed as

$$\alpha_{si} = -\frac{1}{\rho_{si}}\frac{d\rho_{si}}{dT}. \tag{6}$$

The effective properties ϕ_b, saline ice density ρ_{si} and expansion coefficient α_{si} are shown in Fig. 3. Note that these are computed on the basis of the assumption that the saline ice does not loose any salt, and that the ice expands as a whole, without expelling brine. In reality, the freezing and expansion process will always imply the expulsion of some

brine (Marchenko and Lishman, 2017), and hence the curves should be viewed as upper bounds of brine porosity ϕ_b and density, and as lower bounds of the effective thermal expansion coefficient (which is, for saline ice, shown with opposite sign). The upper bound, based on complete expulsion of brine, is the expansion coefficient of pure ice (Cox, 1983) shown as a black stippled line. Note that, for moderate to high solute concentration, the expansion coefficient is dominated by porosity changes during cooling and equilibrium freezing (see Fig. 3). Because $\phi_b \sim S/T$ the expansion coefficient roughly scales as $\sim S/T^2$. E.g., at 30‰ and −15 °C the (negative) effective saline ice expansion is still 3 times larger than the expansion coefficient of pure ice.

In the present study we also used aqueous CsCl solutions, as these allow for a better X-ray contrast and segmentation of the ice-brine 3D images. For CsCl, and mixtures of CsCl and NaCl, the liquidus relationships ($T_f = f(S)$) differ from the above Eq. (A.1), with corresponding changes in the effective densities. In the present study we do not account for all these details. Instead, we simplify the presentation of results by assuming that the freezing point depression, being a molar property, is reduced for CsCl by the ratio of molar weights of CsCl and NaCl ($168.36/58.44 \approx 2.88$). Hence, we plot results obtained for a CsCl concentration X in comparison to a NaCl concentration of $X/2.88$, and do a simple weighting for mixtures.

2.3.2. Porosity metrics

As discussed in recent work on sea ice microstructure (Maus et al., 2021; Salomon et al., 2021) it is useful to define several porosity metrics, in addition to the brine and air volume fractions ϕ_b and ϕ_a. These are the brine porosity open to any of the samples surfaces, ϕ_{op}, the vertically connected brine porosity ϕ_{zz} (open to the upper and lower ice surface), and the closed brine porosity ϕ_{cl} not open to any surface. We also define a dead-end porosity ϕ_{de} (open to only once ice surface). The relationships between the four brine porosity metrics are
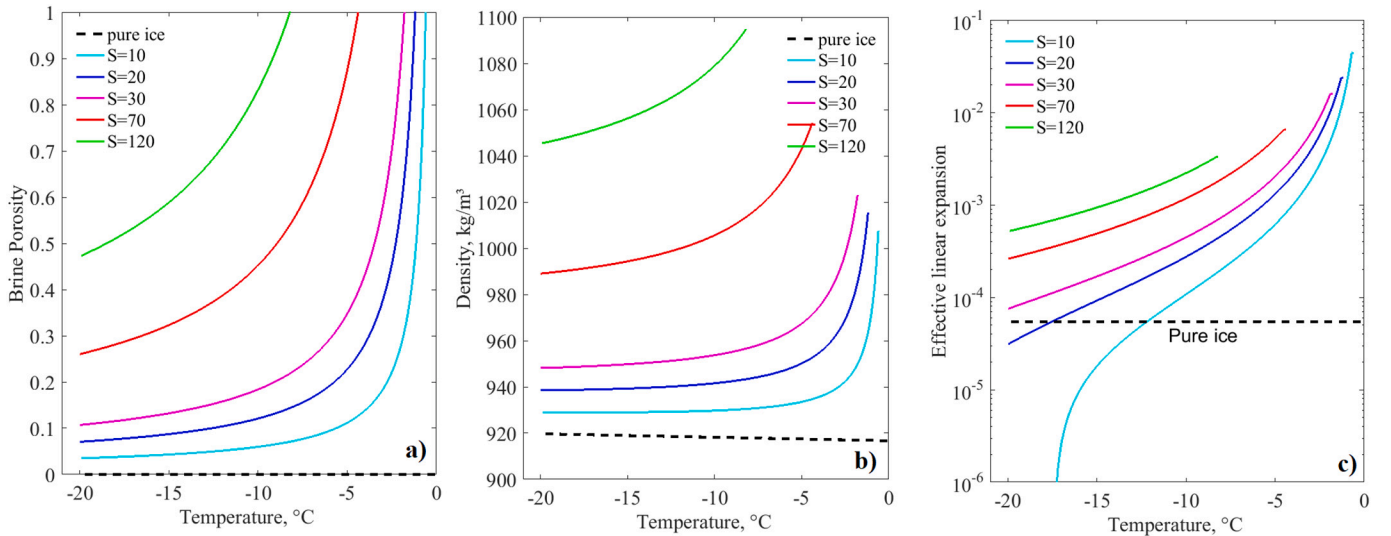
$$\phi_{cl} = \phi_b - \phi_{op} \tag{7}$$

$$\phi_{de} = \phi_{op} - \phi_{zz}. \tag{8}$$

All these metrics can be obtained from 3D micro-CT images.

2.3.3. Plate spacing and pore sizes

For the present setting of the freezing of thin water layers the in-

Fig. 3. Temperature dependence of effective properties of freezing NaCl solutions for different solute concentrations: a) brine volume fraction ϕ_b, b) effective density of the ice-brine composite, including pure ice and its slight temperature dependence, c) effective linear expansion coefficient of the ice-brine composite (assuming no brine expulsion). Note that the linear expansion coefficients of saline ice are shown with opposite sign - contrasting the pure ice value. The curves for different salinities start at the respective freezing temperatures.

fluence of convection is probably of minor importance. According to Maus (2020) the lamellar spacing a_0 may then be related to the ice growth velocity V in the form

$$a_0 = 1.89 V^{-2/3}, \tag{9}$$

where a_0 is in millimetres and V in cm/day. The equation is strictly valid for seawater and NaCl solutions with solute concentrations similar to natural seawater (30–35‰). While both observations (Lofgren and Weeks, 1969) and theory (Maus, 2007; Maus, 2007) indicate a slight dependence on solute concentration, the latter will be ignored in the present analysis. Note that sea ice scientists are mostly using the terms *brine layer spacing* and *plate spacing* (Nakawo and Sinha, 1984; Weeks, 2010; Maus, 2020), and while we shall henceforth use *lamellar spacing* to distinguish the vertical ice and brine lamellae from the horizontal saline ice layer on top of the concrete.

The essence of the *lamellar spacing* is that it allows, for columnar saline ice, to construct an idealised model of the pore space. This was first proposed by sea ice scientists in the 1960s (Anderson and Weeks, 1958; Weeks and Assur, 1964) and is illustrated in Fig. 4. The internal freezing is simplified into three phases. During the first phase (Fig. 4a to c) sea ice has low strength and the width d of brine lamellae simply changes with porosity as $d = \phi_b a_0$. At some critical width d_0 the brine lamellae start splitting into cylinders (indicated with a wavy pattern in Fig. 4c). At the end of this splitting phase the layered morphology is changed into cylinders of the same diameter d_0 (Fig. 4d). In the third phase (Fig. 4d to e) the cylinders shrink with brine volume, now according to $d \sim \phi_b^{1/2}$. In this phase ice necks are established across the

brine layers, and they grow in width while the cylinders a shrinking. The following Equations quantify this behaviour for different ranges of the brine volume fraction, and in dependence on a_0 and d_0:

$$d = \phi_b a_0, \quad \phi_b > d_0/a_0 \tag{10}$$

$$d = d_0, \quad \phi_{b0} < \phi_b < d_0/a_0 \tag{11}$$

$$d = d_0(\phi_b/\phi_{b0})^{1/2}, \quad \phi_b < \pi d_0 \big/ 4 a_0 \tag{12}$$

where

$$\phi_{b0} = \frac{\pi d_0}{4 a_0}. \tag{13}$$

may be viewed as the critical brine volume fraction ϕ_{b0} when the splitting has taken place, establishing an ice matrix with much higher strength. The challenge is to determine the critical layer width d_0 of this transition. Anderson and Weeks (1958) were the first to address this problem and suggested $d_0 \approx 0.07$ mm on the basis of 2D thin section analysis. Later a value of 0.11 mm has been proposed, based on a structural model of sea ice strength (Weeks and Assur, 1964) and the tensile strength data from Weeks (1961). A recent analysis of micro-tomographic imagery of young sea ice (Maus et al., 2021) indicates a median pore diameter of $\approx 0.12 \pm 0.01$ mm as condition for imperme-able sea ice, when cylinders neck. While more work is needed on this topic, the best estimate of critical width (brine lamellae and cylinder) at the transition seems to be slightly above 0.10 mm. In the present work we shall assume $d_0 = 0.12$ mm.
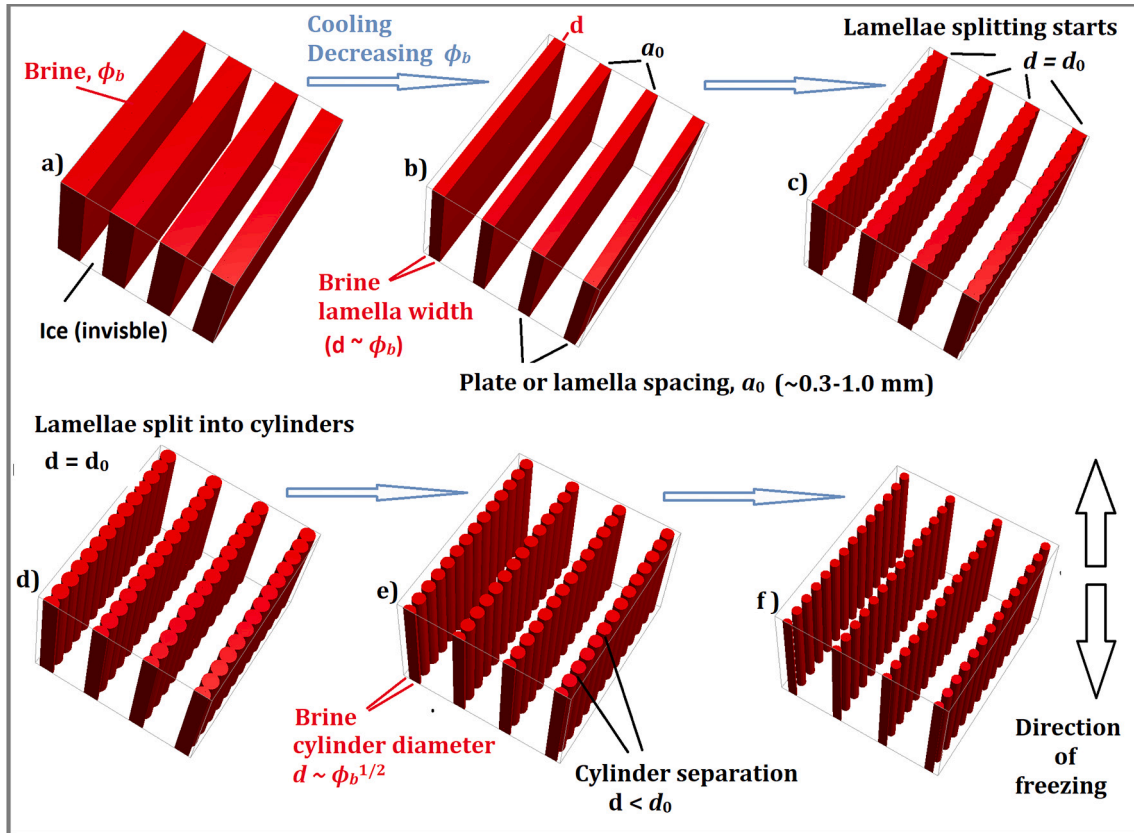
Fig. 4. Schematic of the microstructure evolution during cooling of columnar saline ice as first proposed by Anderson and Weeks (1958). Brine is shown in red, with ice being invisible. During cooling from a) to f) brine solute concentration S_b increases and brine volume fraction ϕ_b decreases. First, from a) to c) brine layer thickness d changes linearly with brine volume fraction ϕ_b. At c) and $d = d_0$ brine layers start splitting into cylinders. At d) brine lamellae are split into cylinders that just touch each other. From d) to e) brine cylinder diameters shrink according to $d \sim \phi_b^{1/2}$. At e) ice necks form in the lammella direction between the cylinders and the strength of the brine-ice-composite is established. Note that the concrete and its interface with the saline ice would be horizontally oriented and normal to the brine layers and cylinders.

In summary, there are two important length scales in young saline ice. The first is the lamellar spacing a_0 that decreases with growth velocity, yet once set is a constant property (*plate* or *brine layer spacing* in the sea ice literature). The second is the width or diameter d of brine channels. This property is not constant, is changing with porosity (and thus with salinity and temperature), and upon reaching a critical width d_0 the brine lamellae separate into cylinders. According to our present knowledge d_0 might be a constant.

2.3.4. Microstructural strength

The two microstructure scales a_0 and d_0 may be incorporated into a structural model of the tensile strength σ of sea ice (Anderson and Weeks, 1958; Weeks and Assur, 1964) that can be written in the form

$$\sigma = \sigma_0 \left(1 - \left(\frac{\phi_b}{\phi_{b0}} \right)^k \right) \tag{14}$$

where σ_0 is a reference tensile strength of pure ice, ϕ_{b0} is the brine porosity at which the strength approaches zero. This transition porosity is, according to the above description and Fig. 4, associated with the splitting of cylinders is given by Eq. (13). In the idealised model the saline ice has no strength for $\phi_b > \phi_{b0}$, while for $\phi_b < \phi_{b0}$ the strength follows Eq. (14). The exponent k is empirical and related to the evolution of the pore space. For the simple case of cylindrical pores of uniform diameter considered above one has $k = 1/2$ and $d/d_0 = (\phi_b/\phi_{b0})^{1/2}$. Inserting the latter expression into the strength Eq. (14) one obtains

$$\sigma = \sigma_0 \left(1 - \frac{d}{d_0} \right). \tag{15}$$

Note that this equation for the structural strength is just based on two length scales - the brine channel width d, a property measurable on CT images, as well as the critical brine channel width d_0 for zero strength defined above.

2.4. X-ray microtomographic imaging and analysis

X-ray microtomographic imaging (micro-CT) of sea ice and saline ice is an evolving technique that has gained attention during the past decade (Pringle et al., 2009; Obbard et al., 2009; Maus et al., 2015; Lieb-Lappen et al., 2017; Maus et al., 2021). In contrast to μCT imaging of snow, the brine content and pore structure in sea ice are strongly temperature-dependent, making temperature-controlled sampling, transport and imaging a challenge. Experience shows that the moderate absorption difference between ice and NaCl brine precludes to a certain degree X-ray imaging with high contrast (Bartels-Rausch et al., 2014; Maus et al., 2021). In the present study we thus complement imagery of saline ice grown from NaCl solutions with observations of ice-brine composites grown from CsCl solutions, yielding higher contrast and image quality.

X-ray micro-tomographic imaging of concrete + saline ice specimen was conducted at the Norwegian Centre for X-ray Diffraction, Scattering and Imaging (RECX), NTNU, with a XT H 225 ST micro-CT system from Nikon Metrology NV, equipped with a Perkin Elmer 1620 flat panel detector with a 2048 × 2018 pixel field of view. Image acquisition was performed with a current source of 260 μA, an acceleration voltage of 120 kV and a Wolfram target. Scans were performed with 3142 rotation per 360 °C and an exposure time of 708.00 ms. The field of view was 55 mm and corresponds to a pixel size of 27 μm. Specimen were placed in an alumina sample holder with 1 mm wall thickness. The top and bottom temperature of the sample holder was controlled by a self-assembled cooling system, based on thermo-electric assemblies (www.lairdtech.com). The temperature during scanning was set to −20 °C, the same temperature as at the end of the freezing test. Nikon Metrology XT Software was used for reconstruction of the data sets. Data were stored as 16-bit grey value stacks. We used the software GeoDict (GeoDict, 2012–2022) for segmentation into the constituents air, brine and ice, and for determination of several porosity and pore size metrics. Fig. 1 shows a grey level image of a horizontal cross section in concrete as well as a side view showing both materials and the interface. The bright ring in the horizontal cross section is the alumina sample holder, and the next inner ring the butyl wrapping around the specimen.

The segmentation of grey level images into air, ice and brine is illustrated in Fig. 5 for a sample frozen from NaCl solution, as well as for a sample where CsCl has been added. For the segmentation we selected a rectangular cross section in a horizontal 2D image to cut out a horizontal cylinder with horizontal side length of 2.5 to 3 centimetres, and a vertical height corresponding to the saline solution layer. While the structures look similar, image quality in ice doped with CsCl is superior in terms of signal to noise ratio and the detection of open and closed pores, in particular for pores that only include a few voxels. For NaCl, where the brine and ice absorption regimes are close to each other, segmentation of brine and ice requires additional information. We thus set the histogram threshold between brine and ice to match the theoretical brine porosity that is expected from temperature and salinity. For the CsCl enhanced images unsupervised segmentation was possible, see also Pringle et al. (2009). However, we use the same method as for NaCl samples - setting the ice-brine threshold to match the theoretically expected volume fraction of NaCl + CsCl ice. Air porosity, with much larger contrast to ice, was manually segmented as described in Maus et al. (2021). Pore and ice structure sizes were then determined with the PoroDict package of GeoDict (GeoDict, 2012–2022).

The uncertainties of the image processing and analysis are similar as recently described for sea ice (Maus et al., 2021) with the following specific limitations in the present study. For air porosity the latter authors mentioned an accuracy of 0.5 to 1%, increasing with porosity, and for the present study the lower end applies. The uncertainty of the brine porosity, with supervised segmentation based on salinity and temperature, is estimated from the temperature uncertainty of the thermo-electric cooling stage (1 °C), resulting in a 0.3 % brine porosity error (based on Eq. (4)). Other aspects of interpreting the present results are related to the limited specimen size. For the specimen frozen with a linear temperature rate (thinnest solution layer of 3 mm, method I) we often had to reduce the vertical extent of the cropped cylinder near the ice-concrete boundary, close to which images were biased by artefacts and strong changes in grey levels. These were created by slight inclination in the vertical axis of the frost salt scaling specimen during scanning, as well as a convex ice surface, both creating beam hardening effects near the interface. We thus typically ended up with less than one mm of vertical dimension of saline ice with stable grey levels that could be easily segmented. However, also for this limited sample height, the principal microstructure results (e.g., lamellar spacing and pore sizes) did not appear to be different when comparing 3 mm to 8 mm thickness for upward growth (see Table 1), and they were still based on several thousands of open and closed pores. The main difference between the pore statistics for similar sample and growth conditions (solute concentration, direction) appears to be related to horizontal rather than vertical variability of pore sizes. As seen in Fig. 5, and Figs. 6 and 9 below, ice crystals (or grains) can be distinguished from each other as areas where lamellae appear as parallel features, corresponding to what is observed for sea ice (Weeks, 2010; Shokr and Sinha, 2015). Pore sizes often vary between grains and tend to be larger at grain boundaries. As most specimen only contain a few grains, this variability is responsible for most of the sample to sample variability in the results presented. Larger specimen sizes, desirable for better statistics, would however have resulted in a coarser spatial resolution (that for our CT scanner is given by roughly 1/2000 of the specimen diameter).

The pixel size of 27 μm defines our spatial resolution and implies, with a Nyquist criterion 2 times the pixel size, that we are able to detect pores with diameters larger than 54 μm. In principle, the pixel size of 27 μm is considered as the uncertainty of all microstructure measures presented below. However, as the smallest pores remain undetected, our
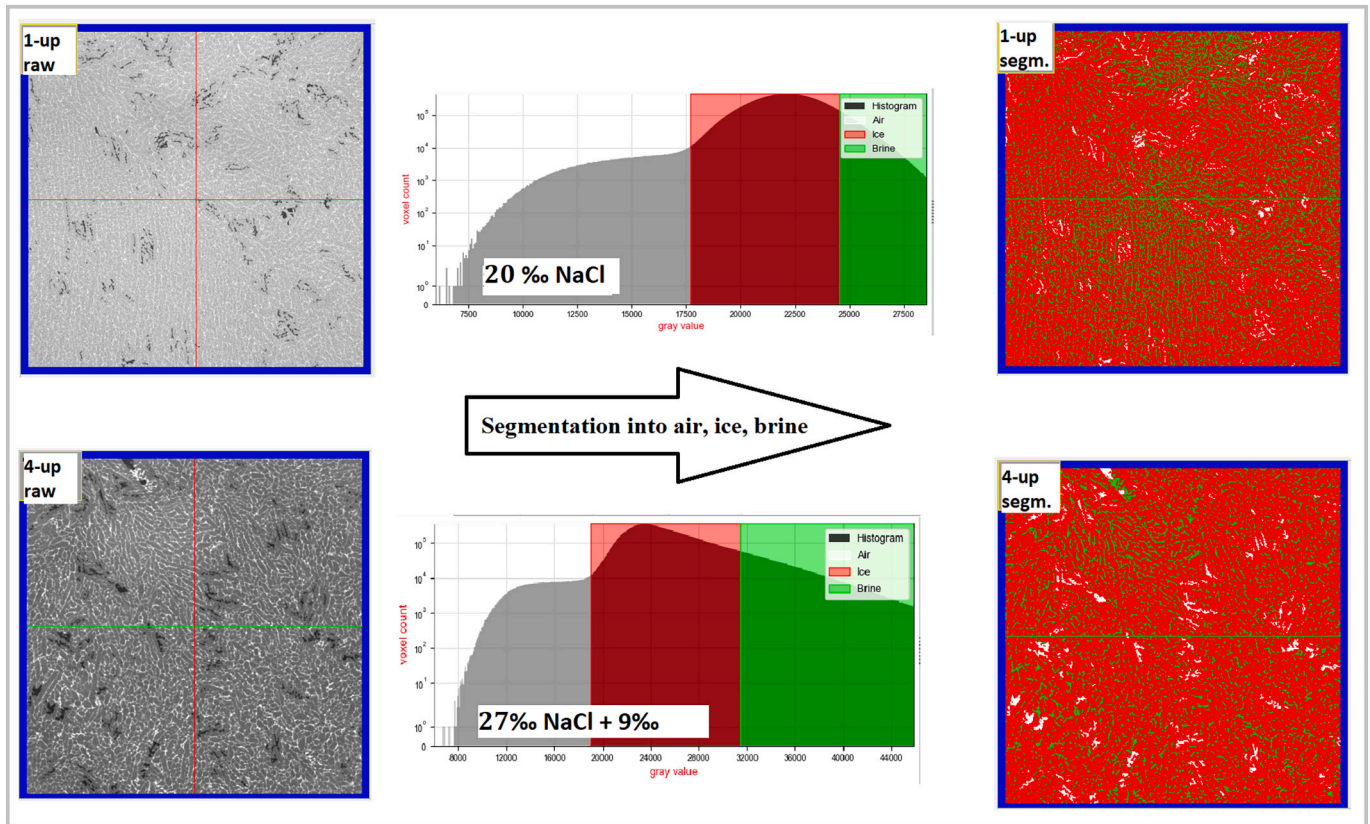
Fig. 5. Horizontal 2D micro-CT images of saline ice, illustrating the segmentation procedure into air, ice and brine. Upper: NaCl ice with low contrast between ice and brine. Lower: CsCl for contrast enhancement. Note that the interface between the saline ice and concrete would be parallel to these images.
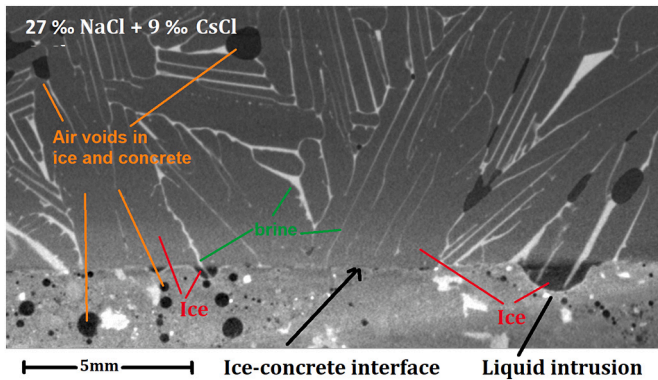

Fig. 6. Grey level micro-CT image cross section of frost salt scaling specimen including both saline ice (upper) and concrete (lower), based on downward freezing of a 27 % NaCl + 9 % CsCl solution (experiment 4-do), and imaged at the final temperature of −20 °C. In the ice, air/ice/brine appear as dark/grey/bright features. Note that both ice and brine pattern near the interface may extend downward from the saline ice into the air pores in the concrete.

median pore sizes are overestimates and only resemble the pores larger than 27 μm. Table 2 lists several porosity metrics (e.g., air and brine porosity, open and closed brine porosities, defined as volume fractions of total sample volume) and pore size characteristics. As in Maus et al. (2021) pore size characteristics were obtained for the pore and ice networks by a sphere fitting algorithm, to determine the fraction of the pore or ice space that belongs to a certain diameter interval. The results from this analysis are the median *brine pore size* D_b and the median *ice structure width* D_s. Note that in an ideal ice-brine composite with just one pore size the measured D_b would correspond to d in our model, while the

Table 2
Porosity metrics and brine lamella/channel characteristics obtained from CT image analysis. Note that d and a_0 (small letters) are the properties in the model, while the equivalent measured properties are D_b and A_0. We distinguish these, because the latter are based on the median values of the pore size distribution, while the former are idealised model properties.

Porosity/pore size metric	Symbol	Description
Brine porosity, total	ϕ_b	Segmented to theoretical value
Critical brine porosity	$\phi_b = \phi_{b0}$	Splitting of cylinders
Critical brine porosity	$\phi_b = \phi_{bc}$	Impermeable, $\phi_{zz} = \phi_{op} = 0$
Open brine porosity	ϕ_{op}	Open to upper or lower surface
Connected brine porosity	ϕ_{zz}	Open to upper and lower surface
Dead-end porosity	ϕ_{de}	Open to one surface
Closed brine porosity	ϕ_{cl}	Not open to any surface
Air porosity	ϕ_a	Air pores, either open or closed
Brine channel width	D_b	Median from sphere fitting
Ice structure width	D_s	Median from sphere fitting
Lammelar spacing	A_0	Computed as $A_0 = D_b + D_s$

sum $D_b + D_s$ would be equal to our lamellar spacing a_0. We finally note that, as we were unable to quantify the brine porosity and structure a few pixels from the ice-concrete interface, we only shortly address this vertical variability (in Fig. 14 below). Hence, the present results represent the bulk saline ice. Fig. 6 is a horizontal slice of a 3D micro-CT image, and indicates that the structure is not fundamentally different near the interface. In addition to the pattern of brine and air pores and networks in the brine-ice composite subject to the present study the figure also illustrates features in the concrete.
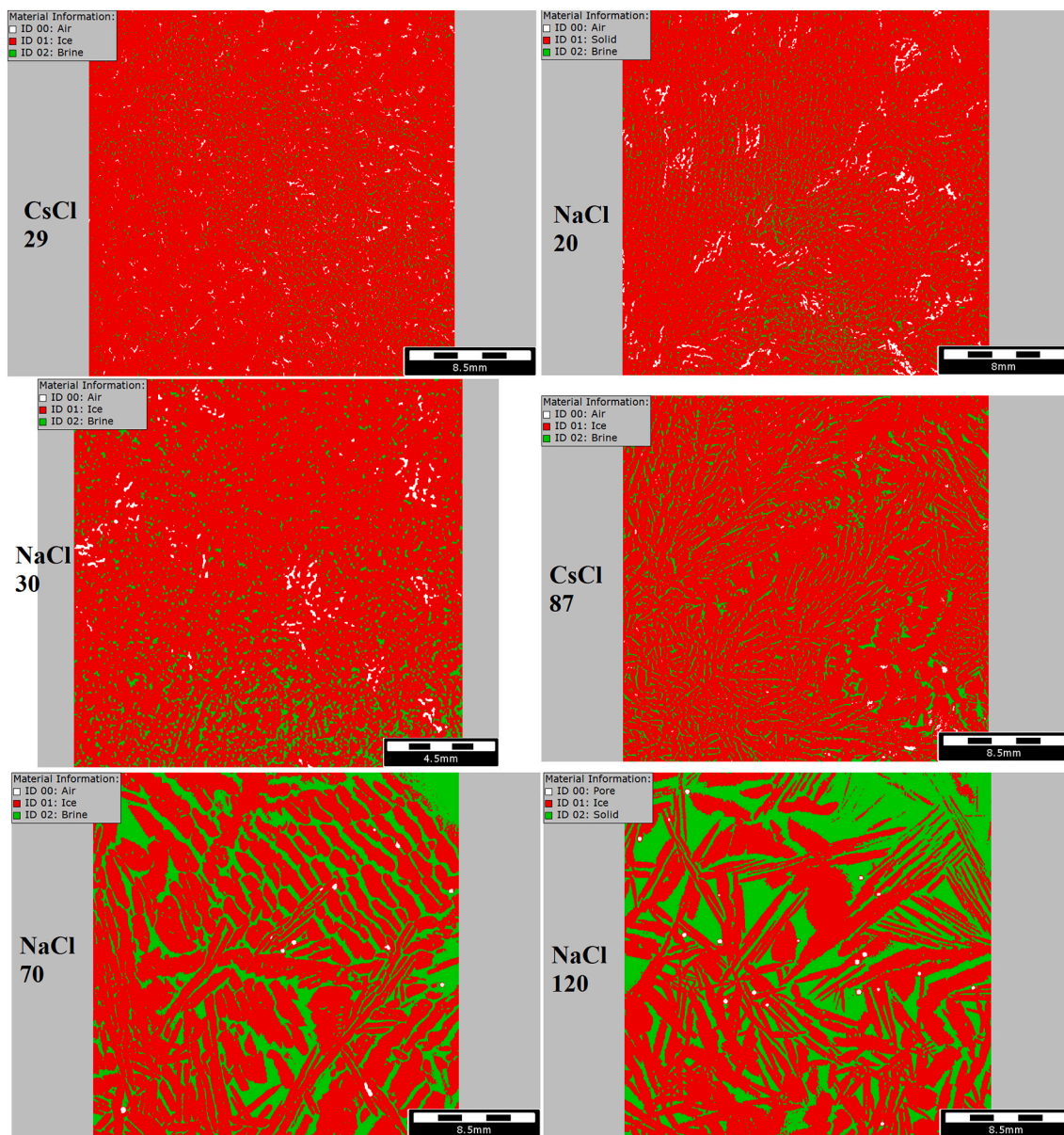
Fig. 7. 2D imagery (horizontal cross-sections) of the brine (green) and air (white) pores in ice (red) in saline ice on top of concrete. The different concentrations of frozen solutions are noted in the figures. All images are obtained at −20 °C. Note that 30‰ NaCl corresponds to 87‰ CsCl in terms of freezing point depression, and that the 29‰ CsCl solution (run 6a) thus corresponds to 10‰ NaCl (run 1b). Note that the interface between the saline ice and concrete would be parallel to these images.

3. Results

3.1. X-ray image analysis

Examples of segmented X-ray micro-tomographic images are shown in Fig. 7 for different solute concentrations that span the range of the present study (10 to 120‰ NaCl). We recall that for ice grown from CsCl solution the concentration needs to be divided by 2.88 to get the corresponding NaCl concentration with comparable freezing point depression and porosity. Several aspects are emphasized when comparing the images. It is evident that porosity and pore sizes are increasing from low to high salinity, with pores at lowest freezing point depression or salinity (29‰ CsCl) being barely visible. We also note that (not shown) pores could be hardly identified in ice frozen from an equivalent NaCl solution (10‰) at our spatial resolution of 27 μm. This is due to lower X-ray contrast of NaCl brine compared to CsCl brine.

When pore widths approach the size of the resolution limit (2 times the voxel size) they are, with low contrast, hard to distinguish from noise. The difference in contrast and sharpness is also apparent when comparing the images for 30‰ NaCl and 87‰ CsCl, with many more details being visible in the CsCl image. Note however, as discussed below, that certain pore size statistics (median) were very similar for these images, and thus could still be derived from 30‰ NaCl ice. This gives credence to our approach to analyse NaCl and low salinity CsCl images together.

Fig. 8a-c illustrates the different connectivity stages of the ice depepending on solute concentration. The upper Figures show the overall texture, while the details are revealed by the enlarged lower Figures. On the left hand side, Fig. 8a is an image of ice grown upwards at moderate velocity with normal solute concentration (27‰). With $d <$ 0.12 mm the brine layers have split into channels, yet one can still see the original brine layers as rows of fine-scale networks. Fig. 8b shows a
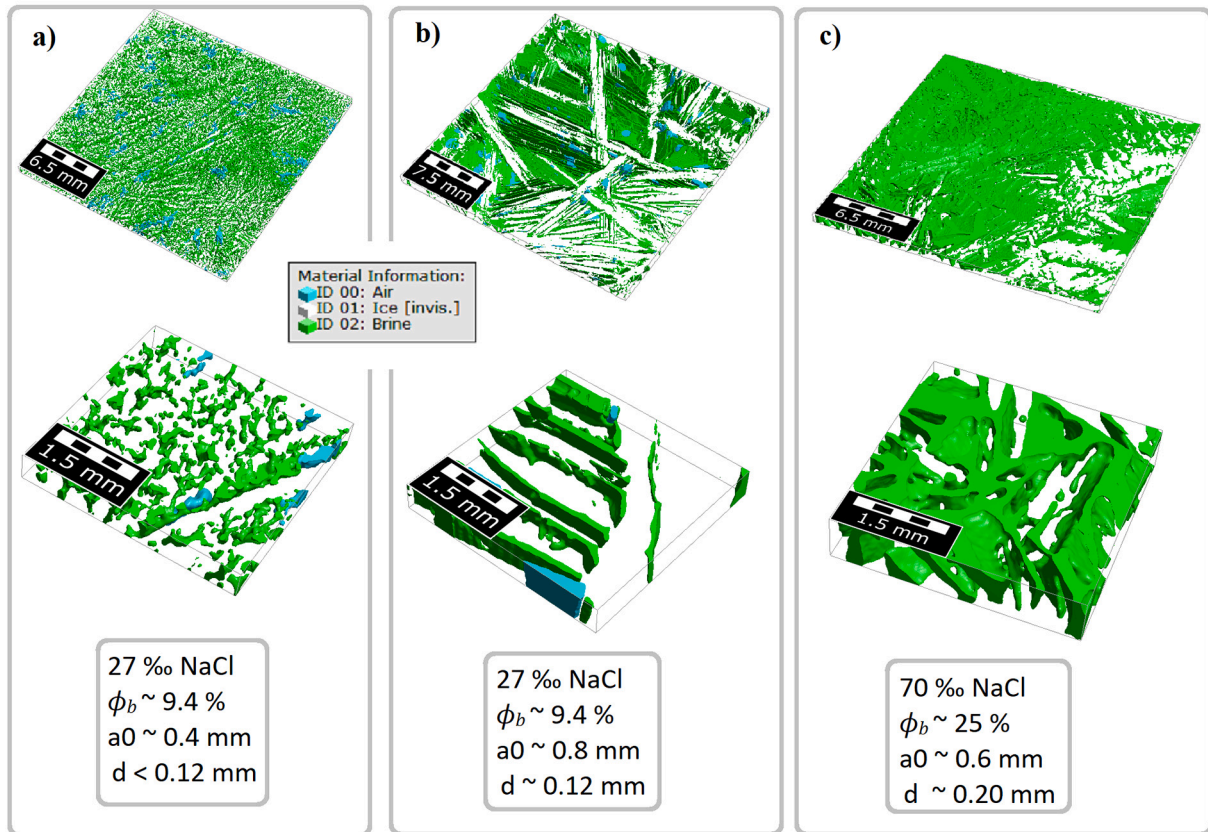
Fig. 8. 3D imagery of saline ice-brine composite on top of concrete with the brine pore space in green, air inclusions in blue and ice being invisible. The images, typical half a millimeter in height, represent different stages with respect to the channel splitting condition (presumably d = 0.12 mm): a) normal solution salinity, rapid upward growth with relatively small lamellar spacing a_0; b) normal solution salinity, slow downward growth with large a_0; c) rapid upward growth yet with a high solution salinity. Note that the interface with the concrete (not shown) would be horizontally oriented located at the bottom of the structures - see also Fig. 20.

sample that has grown downward at lower velocity, giving an approximately 2 times higher plate spacing. The same brine volume fraction is thus contained in half the number of brine layers in Fig. 8a. Here the brine layers are still rather intact, yet one may see some undulations indicating that they are close to the splitting transition. The right hand images visualizes the pore structure of a solution from which ice was grown at intermediate velocity, yet with a higher solute concentration. Here the brine layers are much thicker. The sample is not homogeneous, and at some locations one may see splitting behaviour, but overall this ice is, due to the high brine volume, far from forming disconnected cylinders or brine inclusions.

3.2. Pore size, ice structure width and plate spacing

Pore size distributions for the selected samples shown in Fig. 7 are shown in Fig. 9 for the whole regime of solute concentrations. It is clearly seen that the modal pores size increases with solution salinity, from a mode in the 27 to 54 μm class at 20 to 30‰ NaCl to a mode near 230 μm at 120‰ NaCl. For the lowest solute concentrations in terms of freezing point depression (29‰ CsCl and 20‰ NaCl) we suspect that we are missing the smallest unresolved pores. Setting the threshold by the theoretical brine volume (based on salinity) will thus artificially increase the visible pores, and the median and modal pore sizes that we compute are overestimates. For 30‰ NaCl the results start to be more reliable. In particular the comparison of the distributions for 87‰ CsCl and 30‰ NaCl, equivalent in terms of freezing point depression, shows very good agreement, supporting the hypothesis that it is indeed the molar freezing point depression that determines ice microstructure, irrespective of the solute.

We shall first restrict the presentation to results from the upward growth experiments (1–6 and 1-up to 6-up) and distinguish between NaCl, CsCl and mixed saline solutions. This distinction has been made to ensure that there is no major difference between the freezing of NaCl and CsCl solutions, which we indeed did not find within the present uncertainties. We note that freezing experiments of NaCl-CsCl mixtures also have been successfully used to derive important features of percolation and the permeability of sea ice (Pringle et al., 2009). However, while freezing NaCl and CsCl solutions appear to have very similar microstructure, there are certainly differences. E.g. the density and expansion coefficients shown in Fig. 3 would be different for CsCl brine with an almost three times larger molar mass.

In Fig. 10 we show the median of the most relevant pore and ice structure characteristics obtained from the pore size distributions. Fig. 10a shows that the median brine channel diameter D_b increases close to linear with solution salinity. The green horizontal line illustrates the spatial resolution limit (Nyquist criterion 2 times the voxel size of 27 μm). Below this line the results are not trustworthy, as many small pores remain unresolved. It is clear that D_b must approach zero for low solute concentrations. However, it will not approach zero as a linear function of porosity, as the original brine layers first split into channels and later into spheres. As noted, these transitions are likely associated with critical length scales, yet are not resolved with our spatial resolution.

Fig. 10b further shows the ice structure width, which is the thinnest dimension of the solid ice columns between the brine channels. This property is well resolved with the present spatial resolution. It seems to be largely independent of solution salinity and falls in the range 0.3 to 0.5 mm. An interesting parameter shown in Fig. 10c is an effective lamella or plate spacing A_0 that is computed from the sum of D_b and D_s,
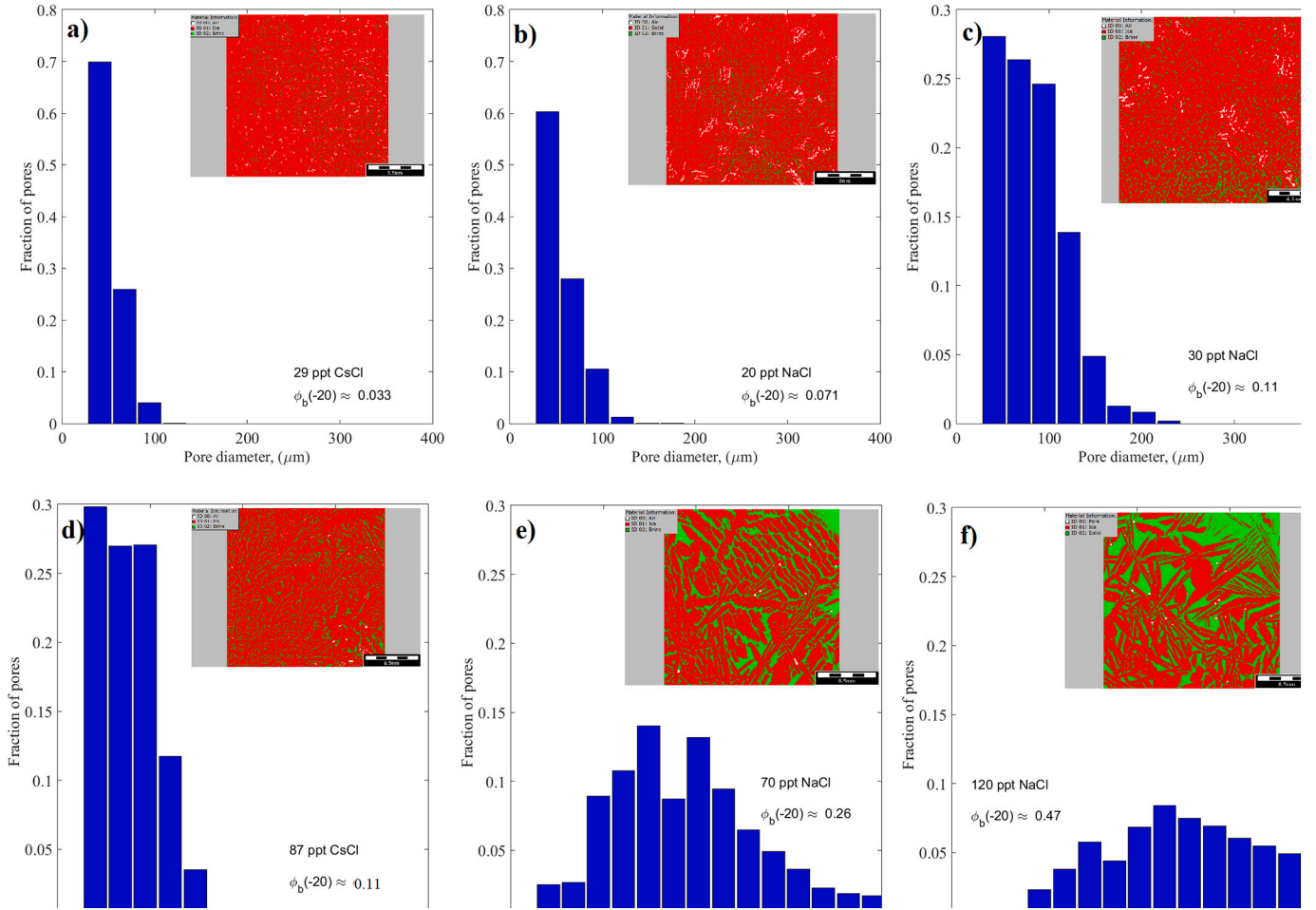
Fig. 9. Brine pore size (channel diameter or width) distributions for different solute concentrations at −20 °C, with inlays indicating the typical pore morphology in horizontal 2D cross sections. Pore sizes increase with solute concentration from a) to f). For the two lowest solute concentrations, a) and b), the distributions indicate that a considerable volume fractions of pores is likely not resolved due to our spatial resolution and the segmentation overestimates the pore sizes. The inlays are the horizontal cross sections from Fig. 7 and illustrate the pore structure.

and that should be related to the lamellar spacing a_0 discussed in Section 2.3.3. A_0 shows a slight increase with solution salinity. Finally we show the relationship between D_b and A_0 in Fig. 10d, and compare it to the straight line ($D_b = 4/\pi\phi_b A_0$), corresponding to the critical diameter d_0 for splitting. Note that this is not the full brine channel evolution model from Section 2.3.3, but just a linear approximation obtained from inserting the observed A_0 and ϕ_b for a_0 and v_{b0} in Eq. (13). Hence, at high concentrations/brine porosity, when brine channel splitting has not taken place, the observations should fall below the dashed 1:1 line, while at low concentrations, when brine channels shrink with $\phi_b^{1/2}$ rather than ϕ_b, they lie above it. At even lower porosity also these channels split and disconnect into spherical inclusions which then shrink as $d \sim \phi_b^{1/3}$. Results are consistent with this principal view of the pore space evolution.

The results presented so far were restricted to upward growth (at constant temperature) and primarily upward growth (linear cooling rate) runs. To put them into a broader modeling frame we now include also the downward growth experiments in the presentation and rather distinguish between growth mode than between different solutes. In Fig. 11a we plot the lamellar spacing a_0 that is predicted from the linear ice growth velocity via Eq. (9) against the observed spacing equivalent ($D_b + D_s$). Reasonable agreement between the predictions and observations is found for all growth modes. We can take the modeling one step further and use the predicted a_0 in Eq. (13) to estimate the brine channel diameter d and compare the latter to the observed D_b. The result is

shown in Fig. 11 b and suggests a high consistency of the model with observations. At the lower end the observations likely are biased to too high values, due to the spatial resolution limit. At the higher end observed brine channels are larger then modeled, similar to the lamellar spacing in Fig. 11a. However, the overall agreement between the simple model and the observed brine pore sizes is remarkable.

3.3. Porosity metrics

The first porosity metric we show is the total brine porosity at the imaging temperature of −20 °C (Fig. 12a). The linear relationship of ϕ_b with salinity confirms the segmentation procedure (grey level thresholding between brine and ice to match the theoretical porosity based on salinity and temperature) and illustrates the distribution of experiments with different solutes.

Of particular interest is the the vertically connected brine porosity ϕ_{zz} in Fig. 12b. Comparison with the total porosity (stippled curve) shows a high degree in connectivity above a solute concentration of ≈ 30‰. At low concentration however (the red squares for CsCl samples) only a small fraction of the pores is vertically connected. For comparison we also show the relationship between total and vertically connected porosity ϕ_{zz} for young sea ice from Maus et al. (2021) that reads

$$\phi_{zz} = 1.05(\phi_b - \phi_{bc})^{1.25} \quad (16)$$
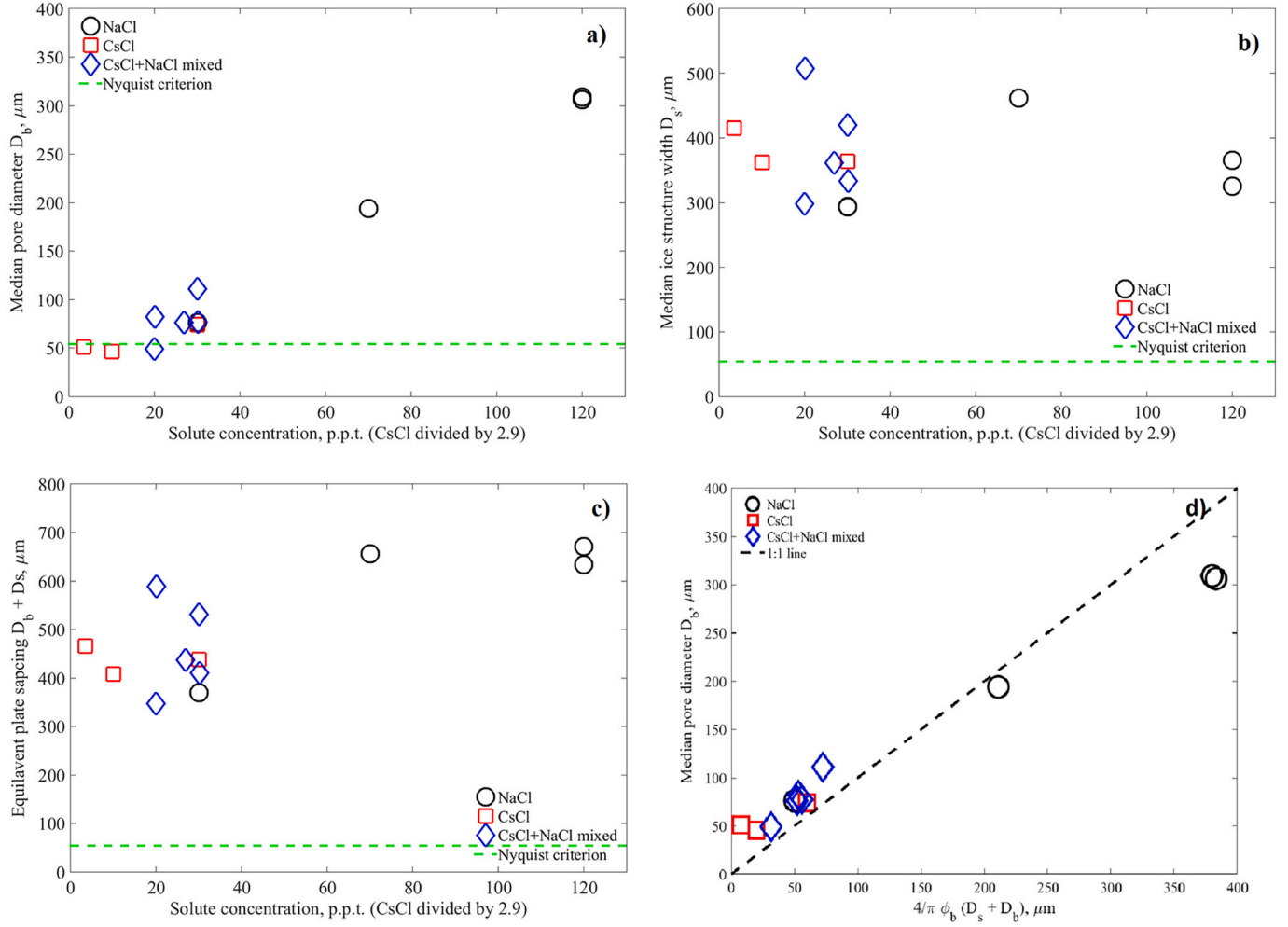
Fig. 10. Median values of pore and ice structure characteristics at −20 °C: a) median brine channel diameter D_b; b) median solid ice structure width D_s; c) median brine channels spacing (from $D_b + D_s$); d) the relationship between brine channel diameter D_b and its prediction based on brine channel spacing.
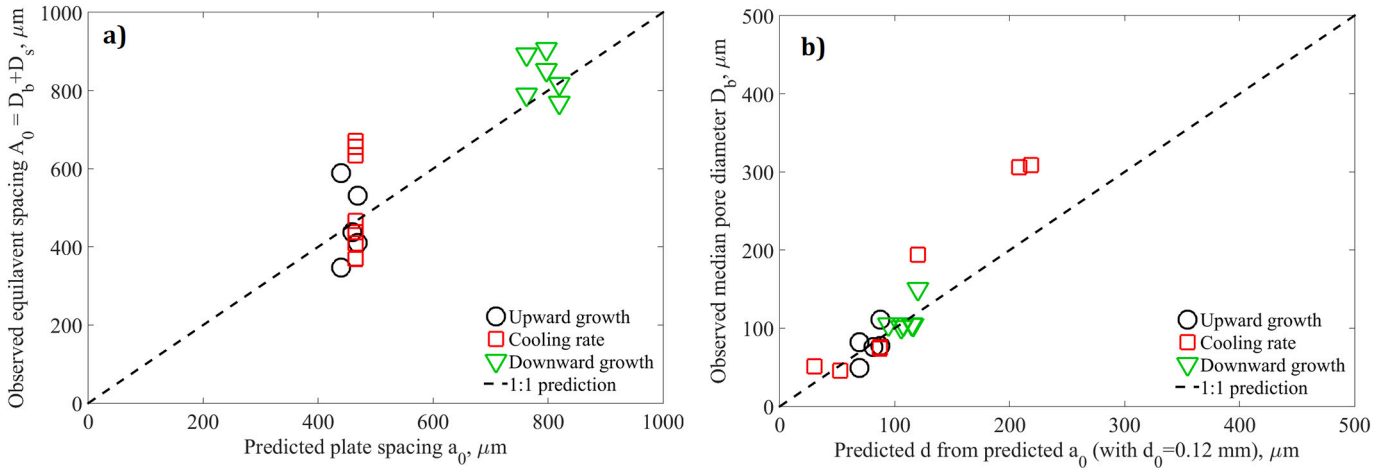
Fig. 11. a) Lamellar brine channel spacing a_0 predicted from growth velocity versus observed spacing A_0 ($D_b + D_s$); b) predicted brine channel diameter d versus observed brine channel diameter D_b.

as well as the open porosity

$$\phi_{op} = 0.569(\phi_b - \phi_{bc})^{0.832} \qquad (17)$$

that includes pores that are open to any side of the sample but do not

need to be connected. The equations give porosities as fractions, not in percent, and are valid down to the critical porosity $\phi_{bc} = 0.024$, below which both open and connected pore fractions become zero. These results were obtained by varying the temperature over the range −2 to −10 °C, in sea ice of lower solute concentration (5–10‰). Here they are
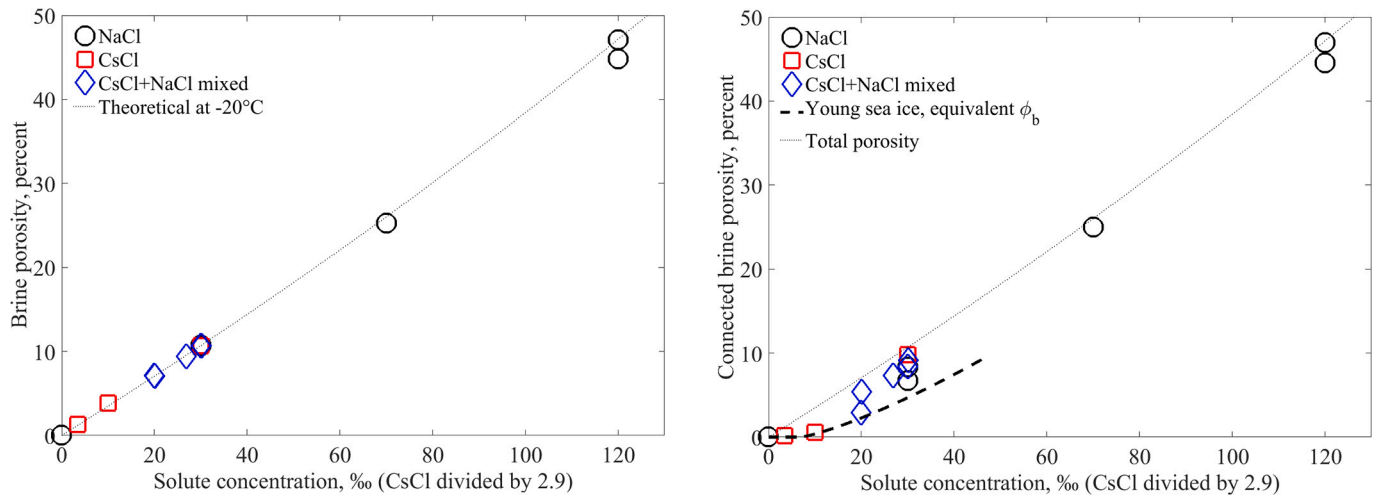
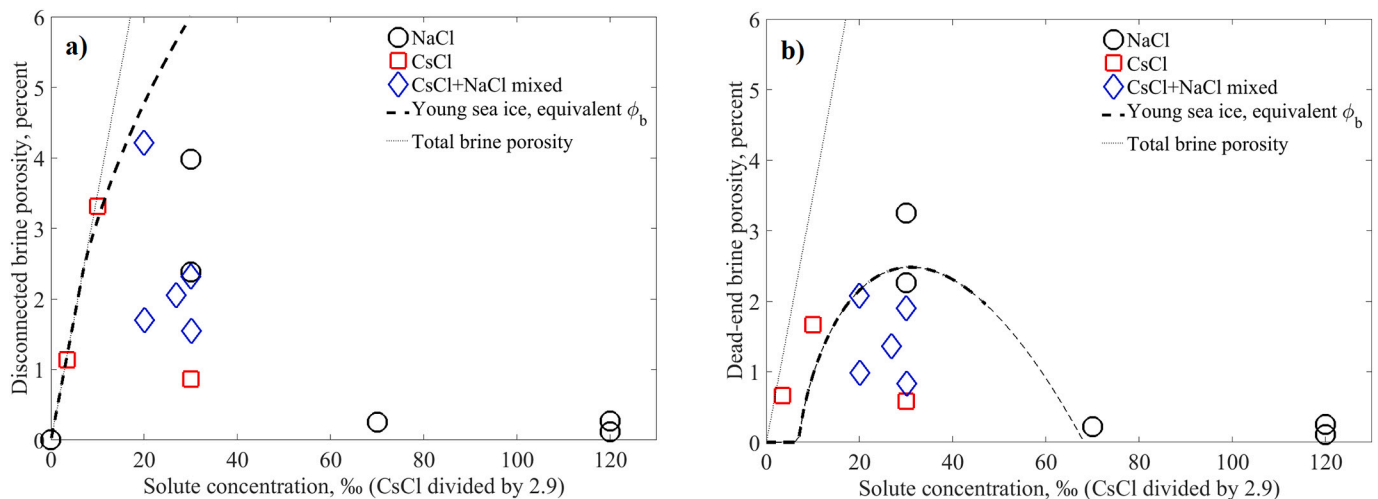**Fig. 12.** a) Total brine porosity and b) Connected porosity versus solute concentration, for the upward growth experiments at the final temperature of -20 °C. The dashed curve in b) shows an empirical fit derived for sea ice at equivalent brine porosity (Maus et al., 2021).

compared to higher solute concentrations at -20 °C, yet at equivalent brine volume fractions. Note that, in this relationship for sea ice, below $\phi_{bc} = 0.024$ all brine pores are closed and ϕ_{cl} becomes equal to the total porosity ϕ_b, while the dead-end porosity ϕ_{de} is zero only by definition. The closed porosity and dead-end porosity depend on pore geometry, pore and sample size. E.g. in a sample with mostly unconnected pores of small diameter compared to sample length, the dead-end porosity just consists of cut pores at the sample faces, and $\phi_{cl} \gg \phi_{de}$. In the presence of vertically elongated disconnected pores, sample cutting may open these pores and result in an observed dead-end porosity that exceeds the closed porosity. The results for sea ice have been obtained for samples of 5.5 mm thickness, similar to the present ice layers on concrete (3–10 mm).

In Fig. 13a and b we compare the closed ϕ_{cl} and dead end ϕ_{de} porosity observations for the present saline ice to the relationships obtained for young sea ice. The sea ice values appear somewhat larger, yet the general agreement is of interest. In particular the dead-end porosity shows an interesting behaviour, in that it first increases with porosity (or solute concentration), reaches a peak near a solute concentration of 20–30‰, and then appears to drop to low values again. Though the sea ice curves are strictly valid only for total brine volume fraction below 20%, and

thus below ~70‰ in our data, and the age of sea ice is several weeks, there is overall agreement.

Finally we report the air porosity ϕ_a for the different experiments in Fig. 14a. Here we highlight the different growth modes, and show results for downward growth with green symbols. Two aspects emerge from the data. First, we find that the air porosity decreases with salinity and reaches a value less than 0.5 % for the 40 and 120‰ saline ice. Second, for the solute concentration range of 20 to 30‰, where 14 samples are available, air porosity is significantly larger for downward growth (1.5 $\pm$ 0.8 %, n = 6) than for the upward growth (1.0 $\pm$ 0.6 %, n = 8). That more air is trapped for downward growth is consistent with the finding of salinity stratification shown in Fig. 14b. We observe an interesting difference between downward freezing and upward freezing saline water layers. For the downward freezing of thicker (10 mm) saline water layers the vertical distribution of brine porosity (and salinity) shows increasing brine porosity towards the ice-concrete interface being roughly two times as large as the average ice value. At the surface, where freezing started, the ice is much fresher, indicating the role of brine convection in a similar manner as for sea ice.

Fig. 13. a) Closed brine porosity (pores without connection to samples surfaces) and b) dead-end brine porosity (pores with connection to only one sample surface) versus solute concentration, for the upward growth experiments at the final temperature of -20 °C. The dashed curves show empirical fits derived for young sea ice at equivalent brine porosity (Maus et al., 2021).
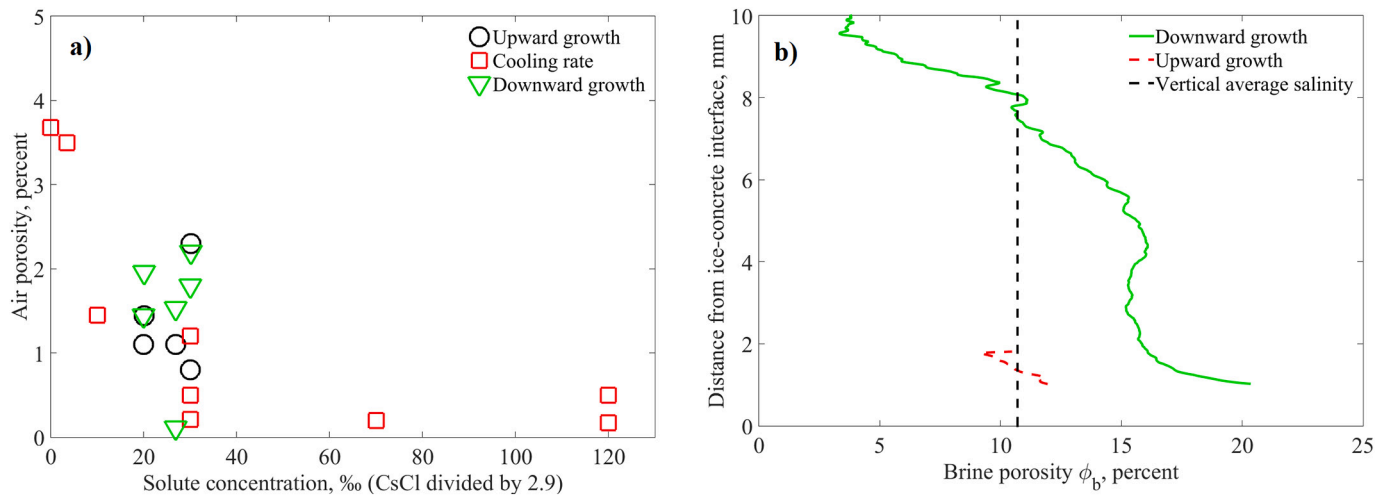
Fig. 14. a) air porosity for different growth modes (upward and downward); b) porosity profile (x = 0 at the ice-concrete interface) showing the difference between a downward freezing 10 mm saline solution and a 4 mm upward freezing saline solution; note that, due to image quality data 1 mm from the interface are not shown.

3.4. Percolation modelling of porosity metrics

The results from Section 3.3 have shaded some light on the behaviour of different porosity metrics, yet the present data are scattered, and the applicability of relationships for sea ice, with different age, thickness and thermal history is unknown. E.g., Fig. 13 shows that the closed brine porosity in sea ice is clearly larger than in the saline ice forming during frost salt scaling. Here we adjust the percolation model validated for sea ice (Maus et al., 2021) to optimally represent the frost salt scaling data and setting. The following model is based on the fractional brine volume (or brine porosity) ϕ_b, rather than on solute concentration.[2] Let us start with the equation

$$\phi_{op} = c_{op}(\phi_b - \phi_{bc})^\beta, \quad \phi_b > \phi_{bc} \tag{18}$$

for the open porosity, in a form that is known to described percolation-based network properties (e.g., Stauffer and Aharony, 1992), in dependence on a critical exponent and a percolation threshold - here a critical porosity. For young sea ice the critical exponent $\beta = 0.83 \pm 0.03$ was obtained (Maus et al., 2021), being consistent with the presently accepted value $\beta \simeq 0.82$ for *directed percolation* (Henkel et al., 2008; Hinrichsen, 2009), which we choose here. For the porosity threshold for the pore space percolation of young sea ice ϕ_{bc} we make the same assumption as for the onset of necking of brine cylinders, that is inversely proportional to the lamellar spacing a_0. Equation

$$\phi_{bc} = f_{bc}\frac{d_0}{a_0} = f_{bc}\frac{4}{\pi}\phi_{b0} \tag{19}$$

sets the percolation threshold as a critical fractional pore volume f_{bc} within the brine lamella that start necking at thickness d_0. Based on $a_0 = 0.56 \pm 0.07$ mm, $d_0 = 0.12$ mm and $\phi_{bc} = 0.024$ for the young sea ice data from Maus et al. (2021) we obtain $f_{bc} = 0.112$. Hence, the channel networks in the brine lamellar become disconnected when their fractional brine volume drops below 11 %, below which $\phi_{op} = \phi_{zz} = 0$. Percolation equations like Eqn 18 are not valid far from the percolation threshold, and in our case we expect that ϕ_{op} will approach the total porosity ϕ_b above the cylinder necking transition ϕ_{b0}. Based on this condition we obtain the constant in equation (18) as

$$c_{op} = \frac{\phi_{b0}}{(\phi_{b0} - \phi_{bc})^\beta} \tag{20}$$

Hence, in the framework of the brine layer transition model the percolation regime extends from ϕ_{bc} to $\phi_{b0} = \pi d_0/4a_0$ where the brine layers consist of parallel cylinders. A similar procedure, yet with different exponent and proportionality constant is applied to derive an equation for ϕ_{zz}. Note that the porosity evolution depends on only two length scales, d_0 and a_0. Similar arguments have been proposed by Petrich et al. (2006), yet were based, due to lack in microstructure data, on a constant a_0 and a different d_0, as well as on an *isotropic percolation* model (contrasting *directed percolation* suggested by Maus et al. (2021)).

In Fig. 15 we present the results for the different porosity metrics versus total brine porosity and focus on the influence of growth velocity. In terms of the plate spacing, and thus growth velocity, the upward growth experiments (red symbols) correspond to the red curves, while the downward growth experiments (green symbols) should be compared with the green curves. Fig. 15a and b for the open and closed porosity show remarkable agreement between the model and observations, also when it comes to the ice growth velocity dependence. This gives credence to the predictions for the high growth velocity (blue curves), for which we do not have observations. Also for the closed porosity in Fig. 15c the data points and model curves agree reasonably. The model curves of ϕ_{cl} show a peak in the closed porosity that corresponds to the growth velocity dependent threshold ϕ_{bc}. Below this value the closed porosity is the same as the total porosity. The predictions of dead-end porosity ϕ_{de} in Fig. 15d show that also ϕ_{de} starts forming at the critical ϕ_{b0} for the brine cylinders. It then increases with decreasing porosity ϕ_b and reaches a maximum, after which it drops again, because now the pore space disconnects while the porosity further decreases. At ϕ_{b0} it is by definition zero, but this cannot be observed on finite sample sizes. We recall that the dead-end porosity is no universal property, but that its magnitude depends on sample size and geometry, in particular the saline ice thickness. The larger scatter in the dead-end porosity, with respect to the predictions, is likely related to variations in the latter. Compared to ϕ_{cl} the dead-end porosity exhibits a different behaviour, with a broader maximum. This is related to the mechanism of pore closure that starts with horizontal splitting of vertically connected cylinders, that would then be classified as dead-end, not as closed porosity. The dead-end porosity increases with growth velocity, as the brine layer spacing a_0 decreases, and thus the number of ice lamellae in a unit volume increases. The overall agreement of predicted and observed porosity metrics is remarkable, supporting the percolation-based modelling, and

---

[2] We note that, as most data were obtained at $-20\,°C$, solute concentrations (in‰) roughly correspond to three times the fractional brine volume (in %).
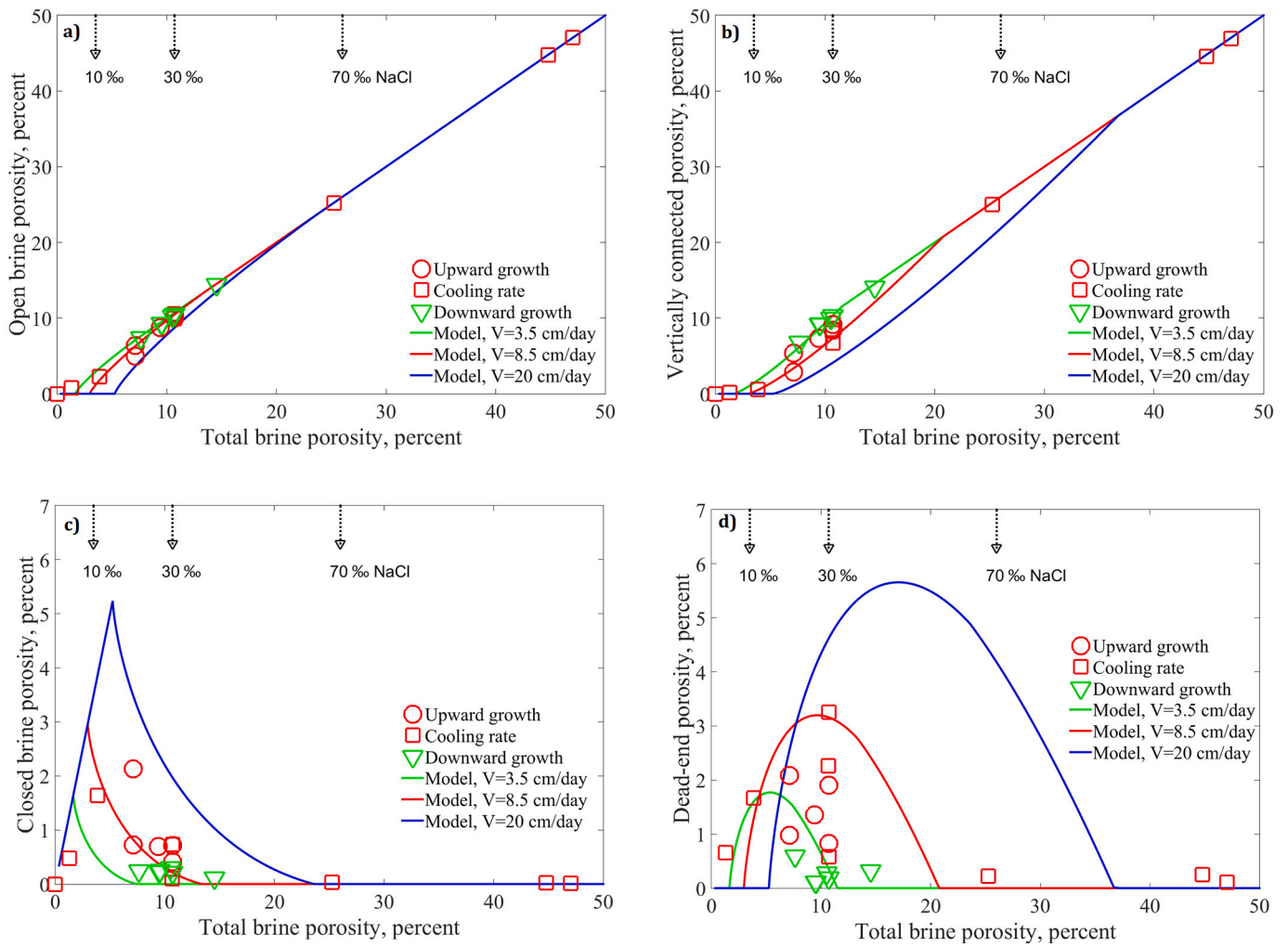
Fig. 15. Modeled versus observed porosity metrics based a) open porosity ϕ_{op}, b) vertically connected brine porosity ϕ_{zz}, c) closed porosity ϕ_{cl} and d) dead-end brine porosity ϕ_{de} for the present salt scaling experiments final temperature of $-20\,°C$, in dependence on total brine porosity, and distinguishing between three ice growth rates. The green and red curves corresponding to downward (green symbols) and upward growth (red symbols) in the present study.
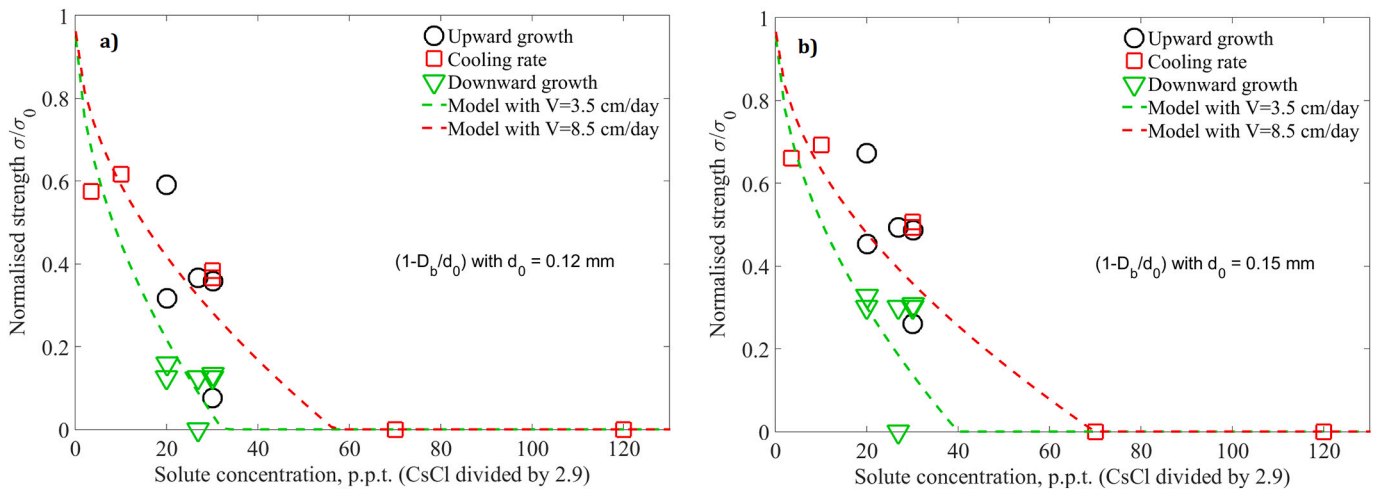
Fig. 16. Normalised tensile strength based on observed microstructure and a simple structural strength model with brine layer splitting at $d_0 = 0.12$ mm (left) and $d_0 = 0.15$ mm (right). Observations are obtained at a temperature of $-20\,°C$, and corresponding brine volume fractions ϕ_b in percent may be obtained by division through 3.

emphasizes the use of model equations to predict further saline ice properties.

3.5. Tensile strength

The microstructure observations allow for the evaluation of the structural model for the tensile strength described in Section 2.3.4. This is done by inserting the observed brine channel diameter D_b for d in Eq. (15). Two values for the transition pore size d_0 (0.12 and 0.15 mm) have been used to illustrate the strength dependence on salinity. In terms of this model, the strength depends on three properties.

- Strength decreases with solute concentration (at fixed temperature)
- The lower the critical splitting length scale d_0, the lower the strength
- Strength decreases with lamellar spacing a_0

In Fig. 16 the dependence of tensile strength on the lamellar spacing is represented by two different growth velocities that imply different spacing a_0. In our experiments the low growth velocities were found during downward growth (green curve and symbols), while higher growth velocities were present in upward growth experiments (red curve and red symbols). Note that we have not measured the strength, but model it based on microstructure predictions, which in turn are consistent with the same model applied to observed microstructures. The results thus illustrate the expected range in saline ice strength provided that the model is correct, and that this range is quite large. The comparison also indicates a better match between modeled strength (the red and green curves) and the observation based strength estimates for the case $d_0 = 0.12$ mm in Fig. 16a compared to $d_0 = 0.15$ mm in Fig. 16b.

4. Discussion

We have performed a detailed analysis of the 3D microstructure of saline ice growing in frost salt scaling experiments. Quantification of characteristic pore sizes and porosity metrics was possible for NaCl solution salinity (or CsCl solutions with the same freezing point) between 10 and 120‰. The relationships between pore sizes and solute concentration are rather robust. The principle microstructure that we find for three cooling and ice growth modes resembles very much what is known from *columnar sea ice*, with a lamellar or sandwich-like structure, where brine channels between thin ice plates are vertically oriented. The spacing of these brine channels (lamellar or plate spacing) is related to the morphological stability during unidirectional solidification of a saline solution, very similar to sea ice[3] (Maus, 2020). However, while for sea ice one often observes a granular layer with random orientation in the upper centimeters, the saline ice in our experiments is columnar right as a whole. This structure facilitates the use of a simplified model to described the microstructure evolution with cooling and decreasing liquid fraction. In addition we have formulated and validated a percolation model that describes the evolution of open and closed porosity in the brine-ice composite. Both properties of saline ice, the microscopic pore scales and the porosity metrics, in turn allow the formulation of parametrisations of mechanical and thermodynamic properties in terms of the fractional brine volume ϕ_b.

The following discussion will extend the results on the microstructure and properties of saline ice with emphasis on the dependence on the ice growth velocity, and the implementation of this dependence in the proposed models for percolation and microstructure evolution during freezing of saline solutions. The microstructure and percolation models can be used to predict many properties (e.g., Sahimi, 1993), and in a recent study we have addressed the hydraulic permeability (Maus et al.,

2021). Here we focus on those properties that are, presumably, most relevant for frost salt scaling at the ice-concrete interface. These are the brine channel diameter (affecting the stress concentration at the ice-concrete interface), the tensile strength and creep of saline ice, the effective coefficient of thermal expansion, and the pore pressure that may evolve due to internal freezing.

4.1. Microstructure and ice growth velocity

The key property of the microstructure of young saline ice is the plate spacing (brine layer spacing, lamellar spacing) and its dependence on growth velocity (Section 2.3.3). This plate spacing is determined by the onset of morphological instabilities during freezing of saline solutions. We have therefore focused on the question how the frost salt scaling set-up affects the ice growth velocity and arrived at reasonable parametrisations of the latter. In our experiments the slowest growth was found for downward growth when air-ice heat exchange is governed by the convective heat exchange in the air (freezer at constant temperature of -8 °C). For upward growth it is the thermal conduction through the concrete layer that (here in connection with a butyl rubber insulation) implied a roughly two times faster growth velocity. The third setting was a cooling scenario often used in frost salt scaling experiments - a linear temperature decrease over time. In our setup the cooling was mostly laterally from the small cylindrical specimens covered by a lid, and ice growth is assumed to be largely upward. In addition to the external boundary conditions also the freezing temperature of the saline solution influences the ice growth. For setups with constant freezer temperature higher salinity solutions are freezing slower.

The growth velocity impacts the evolution of microstructure and properties in several ways. First of all, it controls the lamellar spacing and determines the skeleton of the saline ice matrix (Fig. 11a). At the same time it also controls the diameter of brine channels sandwiched between the ice lamellae (Fig. 11b). When the ice is cooled, its bulk brine volume is subsequently decreased and the brine layers shrink in thickness. As pointed out first by Anderson and Weeks (1958), at a certain width these brine layers/lamellae start splitting into cylinders, and the morphology of the ice is changing. According to the present model, the brine porosity of this transition will increase inversely with the plate spacing a_0 (Eq. (13)), and thus increase with growth velocity. The present model results are compared to the observations in dependence on total brine porosity ϕ_b in Fig. 17. As the the growth velocities in the present study were largely located in two regimes (slow downward and moderate upward growth), the observations are color coded (green and red) in the Figure and should be compared to the model curves with the same colors. The theory apparently predicts the growth velocity behaviour very well. Note that we do not have observations to be compared to the blue high growth velocity curve.

While an analysis of the microstructure of concrete has been beyond the scope of the present study, we can compare the microstructure scales in the ice to some published data. Earlier studies have identified one important length scale, called the *critical spacing factor* L_a or air void spacing. Once defined by Powers (1954), its determination and role has been discussed in detail by Fagerlund (1993), who defined it as 'the biggest piece of a cement paste that can be completely water saturated during a freezing test without suffering any damage'. E.g., Fagerlund reports on an approach to freeze completely saturated concrete and measure the size of the fragments. In practice the spacing factor reflects the spacing of air voids, and values mostly in the range 0.1 to 1 mm have been computed, with frost salt scaling damage of concrete increasing with spacing (Pigeon et al., 1985; Fagerlund, 1993; Pigeon et al., 1996; Hasholt, 2014). This is consistent with the general observation that higher air void content (lower spacing of air voids) prevents salt scaling. As pointed out by Fagerlund (1993) the intrinsic spacing factor is always larger than the critical value, as some of the air voids may be saturated with water. When it comes to diameter of air voids, these are mostly found i the range 0.02 to 0.2 mm with a peak near 0.05 mm (Pigeon

---

[3] Note that for sea ice, due to the effect of solutal convection, slightly smaller lamella spacing is found and predicted (Maus, 2020).
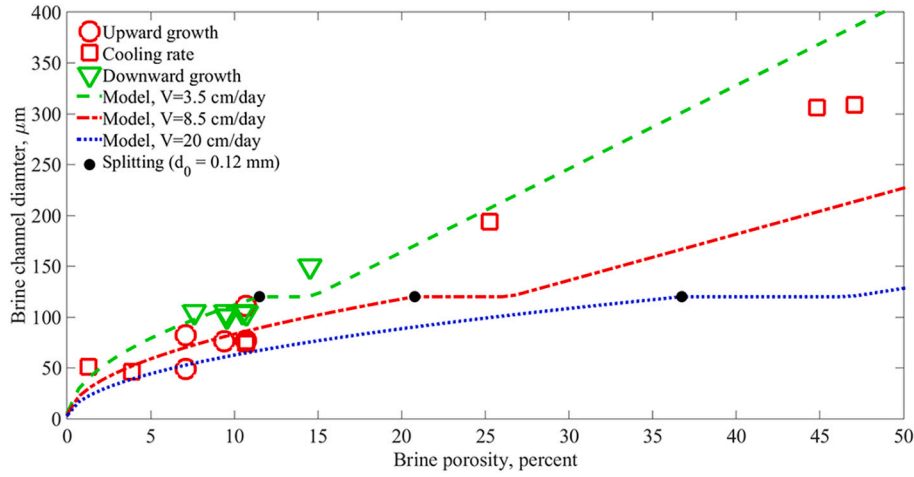
Fig. 17. Modelling the brine layer width d for three different growth velocities and corresponding plate spacing a_0. The observations correspond to low growth velocity (green, downward growth III) and medium growth velocity (linear cooling rate I and upward growth II), while no data exist for high growth velocity. The black dots indicate the porosity ϕ_{b0} for the splitting of brine layers at $d_0 = 0.12 mm$. This porosity depends on growth velocity.

et al., 1996). Hence, the size range of the spacing factor is $(0.1 < L_a < 1$ mm) is very similar to the range of the lamellar spacing a_0 in the saline ice under natural freezing conditions, while brine channel diameters and air voids size ranges are also comparable, around 0.1 mm. This may give rise to mutual interactions between these length scales during frost salt scaling. As an interesting aspect, Pigeon et al. (1985) reported tests where the effective air pore void spacing L_a decreased with cooling rate. Although in these tests mostly internal cracking, and no surface scaling, was observed, they point to the need to a better understanding of critical length scale in both ice and concrete.
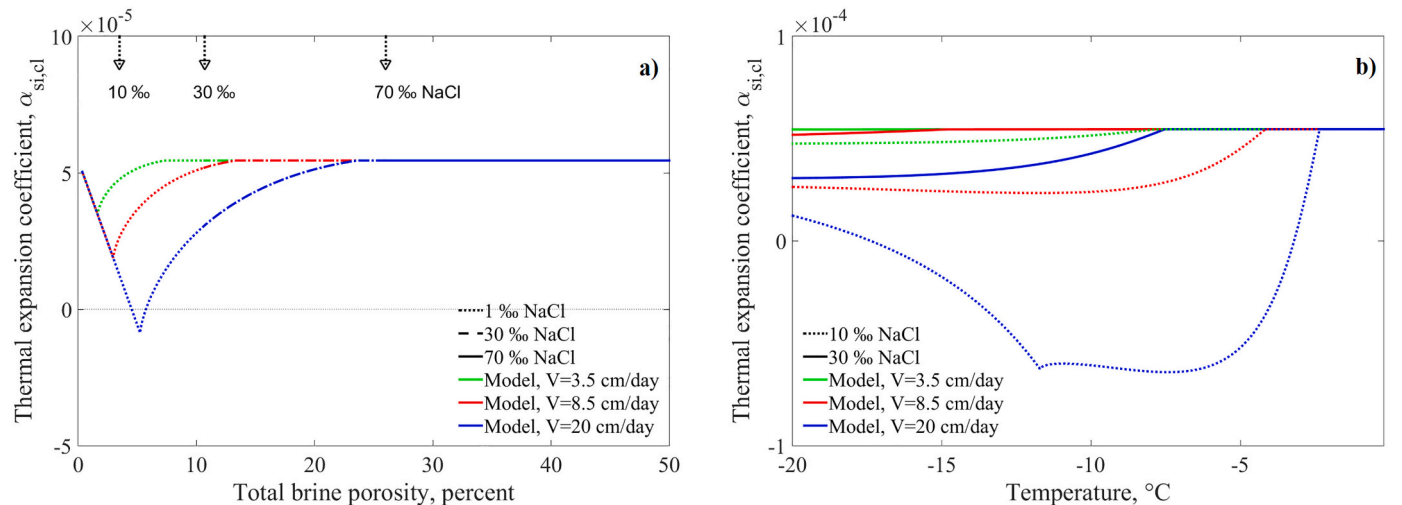
4.2. Effective thermal expansion

Theoretical analysis of thermal expansion has shown two limits. The 'closed container' limit, where thermal expansion is, due to the continous phase transition of brine, negative over much of the natural temperature range (Anderson, 1960); and the 'expelled brine' limit where the volume change due to brine freezing in pores is compensated by brine expulsion, resulting in the hypothesis that sea ice has the same (positive) thermal expansion coefficient as pure ice (Cox, 1983). As pointed out by Marchenko and Lishman (2017) the truth should lie

between these extremes, and the thermal expansion coefficients may be found by partitioning the brine pore space into disconnected and connected pores. Based on our model for the closed and total brine porosity we propose the following equation for a thermal expansion coefficient $\alpha_{si,cl}$ that accounts for closed brine pockets:

$$\alpha_{si,cl} = \frac{\phi_{op}}{\phi_b}\alpha_i + \frac{\phi_{cl}}{\phi_b}\alpha_{si}. \tag{21}$$

Therein α_i is the coefficient of thermal expansion of pure ice and α_{si} the 'closed container' thermal expansion of saline ice given by Eq. (6). For the open, closed and total porosities the condition $\phi_b = \phi_{op} + \phi_{cl}$ applies. Hence $\alpha_{si,cl}$ is a linear average of the pure ice and full brine expulsion limit and the closed ice limit, weighted by the open and closed brine porosity fractions.

The results of the calculations of are shown in Fig. 18 that presents $\alpha_{si,cl}$ in dependence on brine volume fraction and temperature, and for several ice growth velocities and solute concentrations. The curves are based on calculations that start at the freezing and then move from high to low temperature/brine volume fraction (from right to left). The solute concentrations at corresponding to the lowest brine volume (at-20 °C) are indicated at the top of Fig. 18a, while Fig. 18b shows the

Fig. 18. Modeled effective linear thermal expansion coefficient of saline ice a) versus total porosity and b) versus temperature, shown for three solute concentrations and three ice growth rates and minimum temperature of −20 °C. The green and red curves corresponding to slow (green symbols) and intermediate growth (red symbols) in the present study.

corresponding evolution with temperature. For medium growth velocity (red curves) a decrease in expansion coefficient is almost absent for solute concentration of 30‰ and higher. An interesting results, contrasting the 'closed container' result in Fig. 3 is that the coefficient of thermal expansion for low enough solute concentration first increases with temperature lowering, and then increases again. It is also interesting that the thermal expansion depends on microstructure. The effect of closed pores - the deviation from the pure ice thermal expansion - increases with growth velocity (from green over red to blue curves). It needs to be noted that the percolation result here describes the brine entrapment and close porosity evolution during the first cooling cycle. In natural sea ice there are hysteresis effects due to cyclic cooling and warming, known to imply Ostwald ripening convection processes, and the formation of wider pores. In terms of our simple model this implies that, driven by solute redistribution by convection and diffusion, some cylinders increase in diameter while others shrink, broadening the pore size spectrum (e.g., Maus et al., 2013). This means that the original brine layers are not perfectly re-established during warming, but that some pores remain disconnected, while others have widened. Hence, when the ice is warmed again, the closed porosity will likely not be completely reconnected, and there will be also disconnected pores at high temperatures and brine porosity, that in turn will lower the thermal expansion coefficient. The young sea ice data set discussed above (Maus et al., 2021) indicates such behaviour. Data on the effective thermal expansion are rare, yet the few existing studies are consistent with this influence of close porosity on thermal expansion at high temperatures (Johnson and Metzner, 1990; Marchenko and Lishman, 2017). In particular (Johnson and Metzner, 1990) found hysteresis in the thermal expansion during a warming-cooling-warming cycle that is of the same order of magnitude then the present predicted effect. As the thermodynamic setting sea ice differs from those for frost salt scaling in terms of solute concentration, ice layer thickness, time scales mechanisms for solute redistribution (brine convection dominating in sea ice) a comparison needs to take this into account. If the ice-brine layer completely melts during thermal cycling, thermal hysteresis in the ice will be absent. In any case, the results in the Figure should be viewed as upper bounds for the coefficient of thermal expansion of saline ice brine composites for frost salt scaling problems.

4.3. Tensile strength, visco-elastic stresses and creep

It is well established that the strength of many porous media is increasing with decreasing porosity. Proposed relationships are a power law $\sigma \sim (1 - \phi_b)^n$, exponential $\sigma \sim exp(-c\phi_b)$, logarithmic $\sigma \sim ln(\phi_0/\phi_b)$ to linear $\sigma \sim 1 - a\phi_b$ (e.g., Li and Aubertin, 2003; Zhang and Jivkov, 2014). As outlined in in Section 2.3.4 above, a linear model has been proposed for sea ice half a century ago (Anderson and Weeks, 1958; Assur and Weeks, 1963; Weeks and Assur, 1963). These authors have put the strength modelling of sea ice into a simple framework that can be tested by microstructure data. While at that time observations based on 2D thin sections were insufficient to validate models, this is now possible on the basis of 3D micro-CT data as obtained in the present study. For evaluation of model results shown in Fig. 16 in a quantitative manner, one needs strength test data with simultaneous measurements of microstructure, in particular the plate spacing a_0. For the tests by Weeks (1961) indeed such measurements are available, were discussed by Weeks and Assur (1963) in connection with sea ice properties, and considered in models for frost salt scaling (Valenza and Scherer, 2006). However, these were ring-tensile strength tests, and this test type is no longer considered to properly represent the tensile strength of sea ice (Weeks, 2010). The only thorough study of tensile strength with reported plate spacing appears to be the work by Dykins (1969), who reported a plate spacing of 0.4 ± 0.05 mm. The full data from Dykins have been analysed by Richter-Menge and Jones (1993) with a similar model as in Section 2.3.4, resulting in $\sigma_0 \approx 1.3$ MPa. In Fig. 19 we show the microstructure observations and model results from Fig. 16, but now

plotted versus the brine porosity. Results are shown for a critical $d_0 = 0.12$ mm, and three growth velocities (that correspond to plate spacings $a_0 = 0.26, 0.38$ and 0.82 mm). The data from Dykins (1969), tensile strength versus total porosity, were taken from Richter-Menge and Jones (1993). The asterisks in Fig. 19 stand for the average of 27 to 47 tests, with relative confidence bounds of 10 %. With the observed $a_0 \approx 0.4$ mm these results from Dykins (1969) should be compared with the intermediate growth rate (red curve) and indeed good agreement is found, in particular at higher porosity. Other authors, with a much lower number of tests, found either slightly larger or lower strength values, yet the plate spacing was only very broadly determined (0.5 to 1.0) mm. The strength data from Dykins (1969) thus can be viewed as the best available reference for tensile strength, and clearly support the present strength model.

According to Valenza and Scherer (2006), tensile strength is a critical parameter in the so-called *glue spall* mechanism for frost salt scaling. Due to that hypothesis surface damage in concrete is created by cracking in the saline ice. These cracks are proposed to form when the stresses due to thermal expansion mismatch of saline ice and concrete exceed the tensile strength of saline ice. Originally the problem was described for glass–epoxy bonds (Gulati and Hagy, 1982). To extend it to saline ice, Valenza and Scherer (2006) noted the need to include creep relaxation of stresses in the ice, and proposed the following characteristic equation for the tensile stress σ_{ci} in the ice close to the ice-concrete interface:

$$\sigma_{ci} = \int_{T_e}^{T_f} \frac{E}{1-\nu} \left(\Delta\alpha - \frac{J_c\sigma_{ci}^3}{dT/dt} \right) dT. \tag{22}$$

Here E and ν are Young's modulus and Poisson's ratio of ice, $\Delta\alpha$ the mismatch in thermal expansion coefficients between ice and concrete, dT/dt the rate of cooling and $J_c\sigma_{ci}^3$ a stress-dependent creep rate.[4] Several properties in Eq. (22) vary with temperature. In particular the solid fraction ϕ_s increases with decreasing T which implies that the ice consists of portions that start straining and creeping at different temperatures. To obtain the stress at final temperature T_e one needs to integrate from temperature T_f to the minimum T_e. In the Appendix A we derive an approximate analytic solution that gives the stress at ice-concrete boundary in dependence on freezing temperature T_f (and thus solute concentration), minimum temperature T_e, Elastic modulus E, cooling rate dT/dt and parametrisations of creep.

Fig. 20 illustrates the visco-elastic stresses, as we may expect them to act on the ice lamellae, assuming that the samples are frozen with their lower side to concrete. In Fig. 21a and b the calculations of the visco-elastic stresses with Eq. (22) are compared to the present predictions of the structurally controlled tensile strength σ_t (see Fig. 19). The calculations are based on the thermal expansion coefficient, elastic modulus and creep of pure ice (lamellae). Fig. 21a shows the evolution of stress and strength with temperature, while Fig. 21b compares the relationship of tensile strength and brine porosity with the maximum visco-elastic creep stress at the final temperature $T_e = -20$ °C. Results for visco-elastic stresses are shown for the two cooling rates 5 K/hour (upper solid line) and 0.5 K/hour (lower dashed line). The different curves indicate a wide range of conditions, depending on solute concentration, ice growth rate and cooling rate. Note that the creep stress computations have been initiated at the freezing point of the solutions, as here the ice lamellae start forming and expanding in contact with the concrete surface. However, this implies always larger initial stresses than the tensile strength. Shifting these curves to lower temperatures, when tensile strength is established, for example the cylinder splitting, might be more logical. In that case it would be also the visco-elastic stress that during cooling first increases more rapidly than tensile strength, followed by a slower increase, and finally at lowest

---

[4] A dependence of creep on stress with exponent ≈ 3 is well established by observations and modelling (Schulson and Duval, 2009).
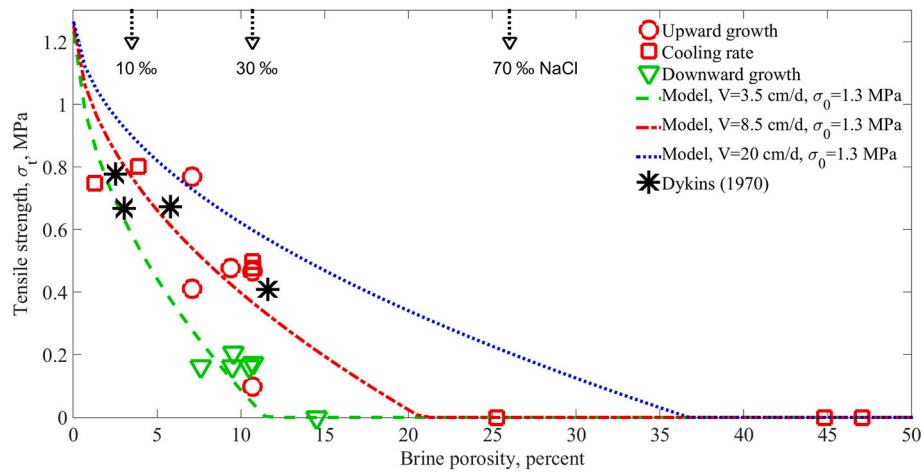
Fig. 19. Strength model results for three different growth velocities, with the green and red curves corresponding to downward and upward growth in the present study. The data from Dykins (1969) correspond to the intermediate growth rate (red) and are compared to normalised model curves scaled by $\sigma_0 = 1.3 MPa$. Note that the observations from Dykins are given with total (air + brine) porosity.
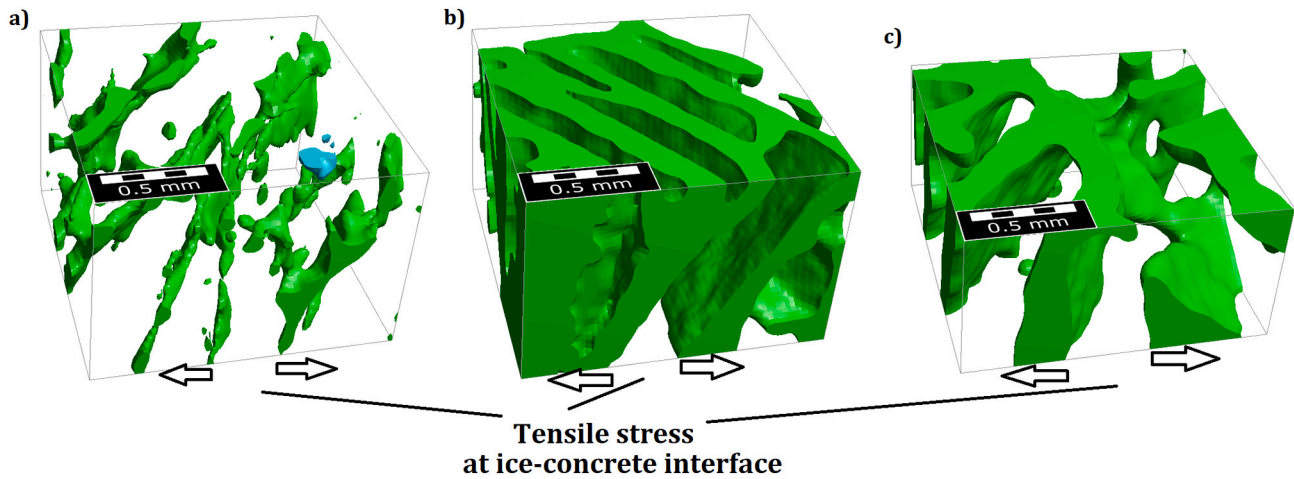

Fig. 20. Millimeter-sized sub-samples from the 3D images in Fig. 8, indicating the location of stresses due to thermal mismatch (assuming the lower side frozen to a concrete surface). Note that brine is shown in green, air in blue, while ice is invisible. The image highlights the different ice and pore morphology for different growth conditions, see caption of Fig. 8. Note that the interface with the concrete would be horizontally oriented and located at the bottom of the structures, with the arrows indicating the stress at this interface.

temperatures a steeper increase. For certain settings (high enough solute concentration and low enough growth velocity) the visco-elastic stress than would raise above the tensile strength. For the larger cooling rate this appears to happen in almost all simulations. Fig. 21 clearly points out the importance of ice growth velocity to evaluate conditions for crack formation.

The visco-elastic stress computations shown in Fig. 21 are based on thermal expansion and creep rates for pure ice, while in the presence of liquid or brine creep has been found to be an order of magnitude larger (Duval, 1977; Riley et al., 1978; Cole, 1998; De La Chapelle et al., 1999). A related aspect is that the saline ice tensile strength, on which the calculations are based, has been obtained in the brittle regime (Weeks, 1961; Dykins, 1967; Timco and O'Brien, 1994), in the absence of creep. However, the (thermal) strain rate during frost salt scaling experiments is 10^{-8} to 10^{-7} s^{-1}, while ductile failure is known to be relevant when strain rates are less than 10^{-4} s^{-1} (Mellor, 1986; Sinha, 1986; Kuehn and Schulson, 1994; Schulson and Duval, 2009). In view of these aspects (Sun and Scherer, 2010) used the static (creep-affected) elastic modulus of the ice-brine composite. We follow this approach and use the relationship proposed by Sun and Scherer (2010) for the static elastic modulus (its dependence on brine volume fraction ϕ_b, Eq. (B.2) in the

Appendix). In addition we employ our formulation for the thermal expansion coefficient of saline ice with closed brine pores, Eq. (21), and we use our microstructure-based strength model. Based on the latter we define the onset of creep stresses for the same brine volume ϕ_{b0} at which tensile strength is established (which happens at different temperatures depending on solute concentration). The results of these calculations are shown in Fig. 22 and indicate a number of interesting aspects. Overall the creep stresses (stippled and dashed curves) are now lower than in Fig. 21, mostly due to the smaller elastic modulus of saline ice. For the lower salinity of 10‰, Fig. 22a, we find creep stresses that exceed the tensile strength only for the case of slow ice growth and faster cooling rate (green dashed curve). The reason is the considerable reduction in the thermal expansion coefficient for medium and rapid growth rates, see Fig. 18. For the higher salinity of 30‰, Fig. 22a, reduced thermal expansion only affects the results at high growth velocities (blue curve), while for the slow and medium ice growth the viscoelastic stresses exceed the tensile strength. It is also interesting to note that the effect of cooling rate on creep behaviour is much weaker in these simulations, because the effective elastic modulus is small (e.g. $\approx$ 1 GPa for 30‰ and $-$ 20 °C). Computations for a solute concentration of 30‰ show that creep stresses never exceed the tensile strength (not shown).
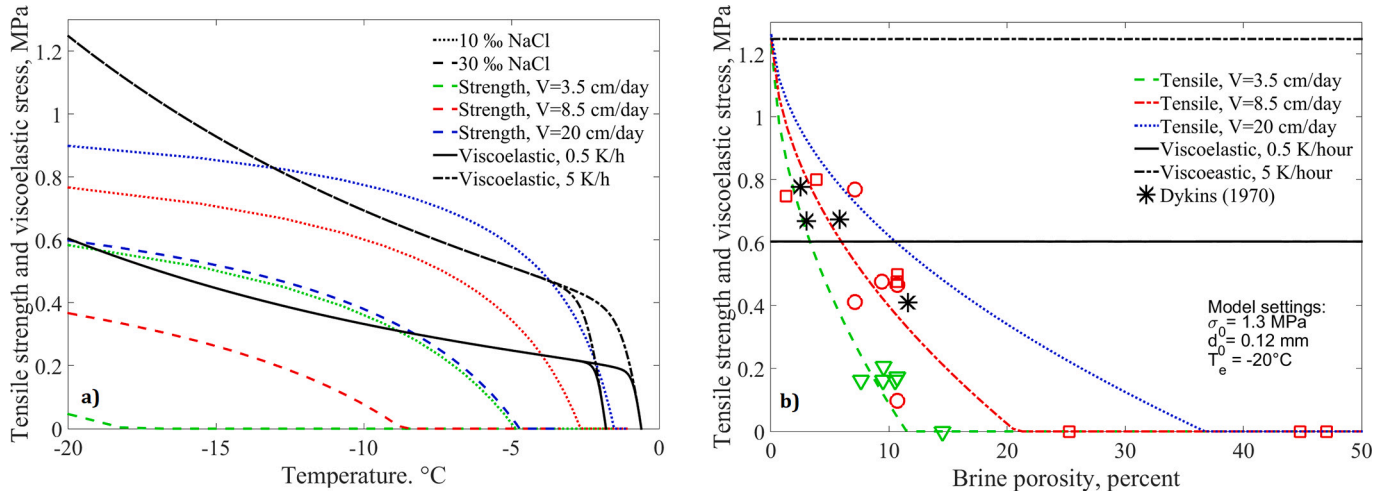
Fig. 21. Comparison of tensile strength to visco-elastic glue-spall stress in saline ice: a) temperature evolution of tensile strength of saline ice growing from two solute concentrations and at three growth rates with visco-elastic stress evolving under two cooling rates. b) tensile strength evolution in dependence on porosity from Fig. 19 compared to the maximum visco-elastic creep stress at minimum temperature $T_e = -20\,°C$. The visco-elastic stresses are based on thermal expansion and elastic modulus of pure ice.
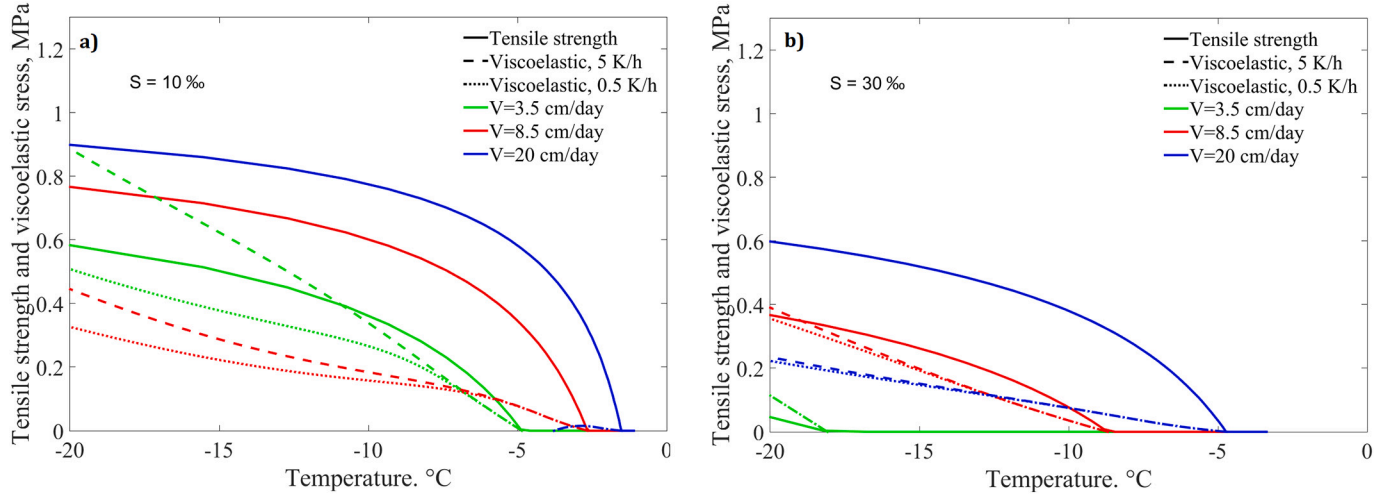
Fig. 22. Comparison of tensile strength to viscoelastic glue-spall stress in saline ice accounting for effective properties of the latter (static elastic modulus, effective thermal expansion): a) for a solute concentration of 10‰ and b) 30‰. Results are shown for three ice growth rates (as in other images shown in green, red and blue) and two cooling rates (dashed and stippled curves).

4.4. Pore pressure

The modeled relationship between dead-end porosity and total porosity (and thus temperature) also allows an estimate of the maximum pressure dP_h that can develop in dead-end pores during freezing. With the bulk modulus K_b for brine (inverse of the isothermal compressibility) the pressure change in dead-end brine pores can be written as

$$dP_h = K_b \left(\frac{d\phi_{de,f}}{\phi_{de}} - \frac{d\phi_{i,p}}{\phi_{de}} \right). \tag{23}$$

The first term in the bracket, $d\phi_{de,f}$, corresponds to the decrease in the volume of brine pores due to partial phase transition of brine to ice, and expansion of the brine-ice composite. The second term, $d\phi_{i,p}$ stands for the increase in the brine pore volume due to compression of the ice phase created by ice pressure dP_i. Assuming that brine pressure creates the same pressure in the ice skeleton

$$dP_i = dP_h = K_i \left(\frac{d\phi_{i,p}}{\phi_i} \right), \tag{24}$$

one can write Eq. (23) in the form

$$dP_h = K_b \left(1 + \frac{K_b}{K_i} \frac{\phi_i}{\phi_{de}} \right)^{-1} \frac{d\phi_{de,f}}{\phi_{de}}. \tag{25}$$

This result corresponds to an effective brine bulk modulus based on the weighted reciprocal average of ice and brine bulk moduli. To predict the hydraulic pressure evolution this equation has to be integrated along the curves for ϕ_{de} in Fig. 15d. These curves include two effects - an increase in ϕ_{de} with lowering ϕ_b due to increasing number of dead-end pores, and the decrease of ϕ_{de} with lowering ϕ_b and temperature due to internal freezing. The latter effect corresponds to $\phi_{de,f}$ in Eq. (25) and may be obtained from

$$\frac{d\phi_{de,f}}{\phi_{de}} = \frac{d\phi_b}{\phi_b} \left(\frac{\rho_b - \rho_i}{\rho_b} \right). \tag{26}$$

It is a function of temperature and brine salinity (through ϕ_b), and densities of ice and brine. Note that the density factor $(\rho_b - \rho_i)/\rho_b$ is ≈ 0.08 for freezing of pure water, yet much larger for freezing of brine (e.
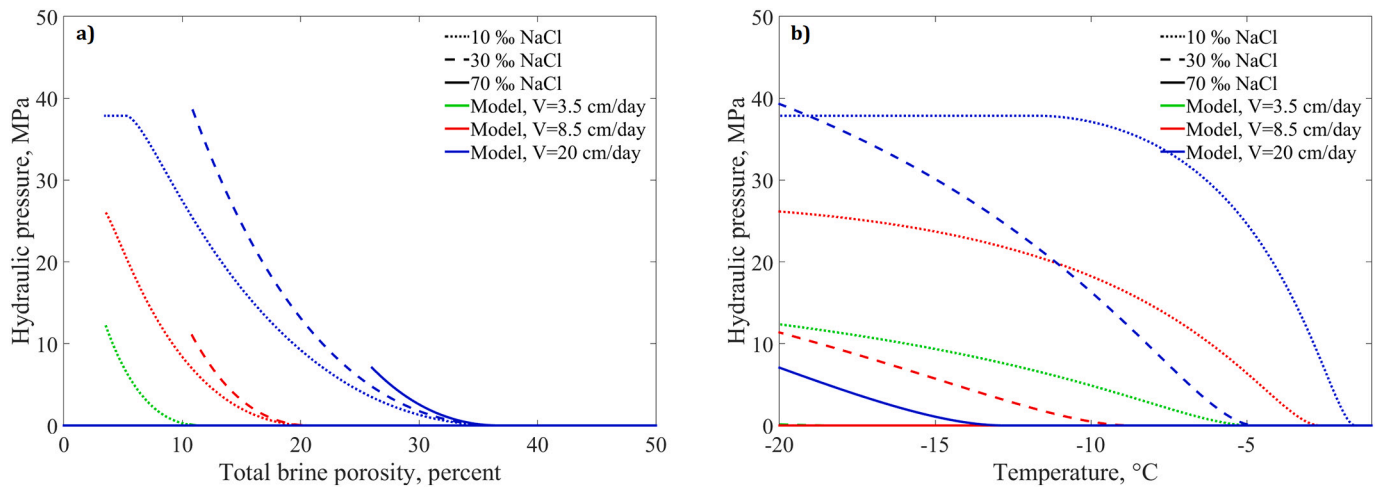
Fig. 23. Hydraulic pore pressure predicted from the change in dead-end porosity a) versus total porosity and b) versus temperature, and shown for three solute concentrations and three ice growth rates. The green and red curves correspond to slow (green symbols) and intermediate growth (red symbols) in the present study. The curves all end at the minimum temperature of -20 °C.

g., ≈ 0.20 at -20 °C). Numerical values for all properties, and their dependence on temperature and brine salinity, that are used in Eqs. (25) and (26), are given in Appendix A.

Fig. 23 shows the hydraulic pressure predicted for the dead-end pores a) versus total porosity and b) versus temperature. As our data fits are for thin ice-brine composites, and roughly half of the dead-end pores are the pores at the lower sample surface, and thus open to the concrete, while the other half is open to the surface, we use half of the ϕ_{de} in the calculations. It is important to note that the results are maximum pore pressures based on the assumptions that (i) Eq. (24) is valid for the pore and ice pressure, (ii) no brine flow into the concrete, (iii) the saline ice does not contain air pores that can be compressed and (iv) creep and thermal expansion of ice are neglected. Though all these processes will likely play a role, and brine flow into the permeable concrete is actually of primary interest, the curves demonstrate the potential effect of hydraulic pressure build-up due to freezing of brine, and its dependence on ice microstructure (solution salinity and ice growth rate). E.g., for the highest solution salinity (solid curves), hydraulic pressure can only build up in ice that has grown very rapidly. For the lowest solution salinity (dotted curves) largest pressures are reached, but this happens at higher temperatures, and one may expect that creep will play an important role when the pressure plateau is reached. Fig. 23a shows that pore pressure starts building up below a critical porosity that corresponds to ϕ_0, cylinder splitting and the onset of formation of closed and dead-end pores. At these points the pressure increases more steeply versus ϕ_b for higher solute concentration - which is explained by lower temperature and higher brine salinity, increasing both the brine density ρ_b and its bulk modulus K_b. To compare the results to sea ice, the results for low and intermediate growth rates are likely of largest relevance. Direct pore pressure observations in sea ice do not exist. However, in a recent study (Crabeck et al., 2019) deduced freezing pressures from visual observations of the evolution of gas bubbles in sea ice. They found pore pressures of up to 7.5 MPa, in principal agreement with the present results.

4.5. Relevance for frost salt scaling: ice growth velocity and concentration pessimum

We have derived and discussed several classes of saline ice properties, which are microstructure length scales, percolation-based porosity metrics and thresholds (ϕ_0 for necking of brine layers, ϕ_c for vanishing permeability), density, thermal expansion, strength and visco-elastic stresses. For many of these properties earlier studies have shown a

strong dependence on total porosity ϕ_b (and thus on solute concentration and temperature), which is clearly confirmed by the present results. The major novel finding of our study is that the properties also depend strongly on the lamellar spacing a_0 of saline ice, and thus on its growth velocity. Furthermore we have, based on 3D microstructure tomographic imagery, formulated a percolation-based framework that allows us to predict several saline ice properties. While an application of these results to model salt frost scaling is beyond the scope of the present paper, we finally discuss two critical aspects of our work. These are (i) the ice growth velocity in salt frost scaling tests and (ii) implications for the solute concentration pessimum (at which salt frost scaling is largest).

Ice growth velocity is not a property that is traditionally monitored in frost salt scaling tests, and so far only the effect of cooling rate has been studied. Though high cooling rates can be expected to imply higher growth velocity (and vice versa), this relationship depends on many factors like the specimen insulation, direction of growth, thickness of water and concrete layers. According to the reviews by Fagerlund (1992) and Jacobsen et al. (1997) there is no univocal relationship between cooling rate and the amount of frost salt scaling in a freeze/thaw test. First studies appeared to indicate that salt scaling increases with cooling rate for uncovered/unsealed specimen cooled in air, while decreasing for sealed samples, which Fagerlund (1992) attributed to the potential effect of moisture absorption. Jacobsen et al. (1997) pointed out that cooling in air makes it difficult to distinguish between the effects of cooling rate and time at minimum temperature. Performing the so called CDF test (Setzer et al., 2007), with the concrete surface facing downward into a thin saline water layer, Jacobsen et al. (1997) found frost salt scaling to decrease with cooling rate. For low cooling rates it was also observed that frost scaling increases with hold time time at minimum temperature, which was not observed for rapid cooling.

Though knowledge on ice growth rates is lacking, we can point out some principal expectations for two frequently used frost salt scaling tests. For the Swedish Standard (SS 13 72 44) slab or Borås test (e.g., Lindmark, 1998), similar to our downward growth experiments 1-do to 6-do, we expect growth velocities at the lower end of our studied range, as the ice growth is controlled by convective heat exchange between air and the saline solution surface. In the CDF test (Setzer et al., 2007) the heat loss from the saline solution is taking place through the bottom of a stainless steel container placed in a temperature-controlled bath. In such a setting the ice growth velocity should principally be larger. Saline ice properties in the CDF test would then be expected in the high ice growth velocity regime (blue curves in Figures), with properties for the Borås test being related to low ice growth velocities (green curves in Figures).

Another principal difference is the direction of saline water layer freezing, being downwards towards concrete in the Borås test and upwards (towards the overlying concrete) in the CDF test. The direction of freezing may affect the saline ice microstructure in two ways. The first is related to the temperature of maximum density, $\approx 4.0\,°C$ for pure water and decreasing more rapid with salinity than the freezing point. For seawater these two are known to match at a salinity of 24.7 ‰(e.g., Sverdrup et al., 1946), with a slightly smaller value of 22.8‰ for a NaCl solution (Kaufmann, 1960; Maus, 2007). Hence, when freezing is downward, thermal convection will only tend to mix the saline solution before the freezing point is reached, if the solution salinity is above this value. This may affect the onset of freezing and the evolving microstructure of saline ice. The second aspect is the vertical stratification of brine within the saline ice (that we observed, see Fig. 14). As brine volume/salinity affect many saline ice properties in a nonlinear manner, the overall saline ice behavior can be different for strong gradients, and properties at the concrete interface may differ for upward and downward ice growth. Both effects, convective mixing prior to freezing and brine redistribution in saline ice, can be expected to depend on the layer thickness of saline water/ice.

The present percolation model of the concentration and porosity dependence of saline ice properties (e.g., strength, pore connectivity) allows some evaluation of the effect of salt concentration on frost salt scaling. Within cryogenic suction studies (Lindmark, 1998; Liu and Hansen, 2015; Müller et al., 2021) the existence of a pessimal NaCl salt concentration has been explained qualitatively by (i) the need of some solute concentration to have brine available for transport into the concrete, and (ii) that increasing freezing point depression at high solute concentration would reduce ice formation and imply less damage.[5] Based on our percolation modelling we can make a quantitative estimate, assuming that the lower concentration bound for frost salt scaling corresponds to the brine percolation threshold, below which the saline ice permeability ceases. Eq. (19) predicts this brine volume fraction ϕ_{bc} to be inversely proportional to the lamellar spacing a_0. For our studied ice growth velocity range $3.5 < V < 20$ cm/day, Eq. (9) gives $0.26 < a_0 < 0.82$ mm, and thus a range $1.6 < \phi_{bc} < 4.7\%$ for the critical porosity. For the temperature of $-20\,°C$ this corresponds to a solute concentration range of 5 to 13‰ NaCl. With regard to the upper solute concentration bound for a pessimum we propose a new idea stimulated by Yener (2015). Consider that the fluid transport into the concrete is not (only) driven by cryogenic suction, but also forced by brine expulsion from the ice. According to our percolation model this requires the existence of dead-end pores which first form below ϕ_{b0} given by Eq. (13). Using the same range $0.26 < a_0 < 0.82$ as for ϕ_{bc} we obtain the range $12 < \phi_{b0} < 36\%$. This porosity range in turn corresponds, at a temperature of $-20\,°C$, to a solute concentration range of 34 to 94‰ NaCl. Both the upper and lower bounds appear consistent with observations of frost salt scaling damage in the range 10 to 100‰ NaCl (Arnfeldt, 1943; Lindmark, 1998; Setzer et al., 2007). Note that the higher values correspond to higher freezing rates – at $V \approx 20$ cm/day the hypothesis would predict upper and lower porosity bounds of 13 and 94‰ NaCl. A similar range has been observed for the CDF test (Setzer et al., 2007) for which we anticipate rapid freezing.

In the glue-spall approach frost salt scaling is either explained as crack formation and propagation in saline ice (Valenza and Scherer, 2006; Valenza and Scherer, 2007; Sun and Scherer, 2010) or, as recently proposed by Bahafid et al. (2022), stress concentration at the ice-concrete interface due to the presence of brine channels. In these theories mechanical properties of saline ice, as tensile strength σ_t, elastic modulus E, thermal expansion coefficient $\alpha_{si,cl}$ and the creep rate J_c play an important role. Valenza and Scherer (2006) explained the salt

pessimum as follows. Thermal expansion mismatch between ice and concrete creates stresses near their interface. At low solute concentrations the tensile strength of ice is too large to be overcome by these stresses, while at high solute concentration there is no strength. Moreover, Bahafid et al. (2022) have recently identified the role of brine channel diameter for stress concentrations at the interface, with wide brine channels (high solute concentration) creating lower stresses. However, the explanation of pessimum effect by Bahafid et al. (2022) remained incomplete due to lack of precise ice microstructure data. The various novel results discussed in the present study provide a basis to extend the approach proposed by Bahafid et al. (2022) and study the pessimum effect in a quantitative manner. The present strength model and visco-elastic creep simulations (Figs. 19, 21 and 22) indicate complex behaviour and a strong dependence of pore scales and properties on ice growth velocity. A detailed analysis cannot be provided here. However, we can use the same basic arguments as for the cryogenic suction approach, and constrain lower and upper bounds for the solute concentration range where we expect salt frost scaling. The upper bound can be related to the brine porosity at which ice strength starts to become established, the ϕ_{b0} for cylinder splitting. As noted above, at $-20\,°C$, this corresponds to a solute concentration range of 34 to 94‰ NaCl. For the lower concentration bound of frost salt scaling we propose another new result of the present study. As shown in Fig. 18, the coefficient of thermal expansion of saline ice decreases with decreasing solute concentration, and may even become negative. Depending, also here, on ice growth velocity and microstructure, the thermal mismatch of saline ice and concrete would become very small below a solute concentration of 5 to 20‰ NaCl (depending on growth velocity), with insufficient stress build-up for damage.

5. Conclusions

The present experiments on frost salt scaling have focused on the microstructure of saline ice that forms from freezing of 3 to 10 mm thick saline water layers on small concrete specimen. The principal results obtained for this microstructure were:

- The saline ice formed has columnar microstructure similar to young sea ice, with vertically oriented brine lamellae and channels.
- Different porosity metrics (closed, connected, dead-end) were also found to be comparable to those observed in young sea ice.
- The distance of brine channels (and of ice lamellae) was dependent on growth velocity.
- The brine channel/lamellae width was, for a giving lamella spacing, primarily related to the brine volume fraction, and thus the freezing point depression. This allows using CsCl as a model for NaCl to achieve higher X-ray contrast (at low solute concentrations).

The analysis and discussion have identified several aspects that appear most important with regard to improvements of salt scaling models and theories. From the viewpoint of saline ice microstructure analysed in the present study we conclude:

- The microstructure scales in the ice-brine composite (pore size, spacing) may be predicted with reasonable accuracy if growth conditions are known, opening new paths of controlled experiments to test salt scaling theories.
- Brine porosity metrics like dead-end porosity, closed and connected porosity of saline ice were determined. Their evolution is consistent with percolation theory and models for sea ice appear applicable to predict them.
- Based on percolation modelling of closed and dead-end porosity and brine expulsion we propose a novel approach to predict two important properties for frost salt scaling - the coefficient of thermal expansion and the freezing-induced brine pore pressure.

---

[5] Recently Müller et al. (2021) proposed that also the chloride binding capacity of concrete plays a role for the cryogenic suction mechanism, by changing the pore solution chemistry.

- Saline ice pore scales and porosity may be used to derive a simple parametrisation of tensile strength and other ice properties; however, interaction between ice microstructure, growth-rate dependent mechanical properties and creep is complex, and validation of theories (e.g., "glue spall") remains challenging.
- The range of length scales observed for the brine channel diameter (mostly 0.1 to 0.3 mm) and brine channel spacing (0.3 to 0.8 mm) are very similar to the ranges of air void diameter (0.02 to 0.2 mm) and the critical spacing factor reported for concrete (0.1 to 1.0 mm), indicating the possibility of their mutual interaction during frost salt scaling (see Fig. 6 for the saline ice concrete interface).
- Percolation-based modelling suggests solute concentration bounds for frost salt scaling mechanisms. For cryogenic suction a lower bound is expected due to a permeability threshold of saline ice. As a mechanism for the upper bound we suggest brine expulsion and pore pressure buildup at sufficiently low brine volume to establish dead-end pores. For the glue spall mechanism a lower concentration bound is consistent with reduced thermal expansion (when disconnected pores are established), while the upper bound relates to the dependence of strength on saline ice microstructure (brine layer splitting).
- Most properties, thresholds and bounds depend strongly on ice growth velocity.

The present model framework of saline ice microstructure and physical properties highlights their role in frost salt scaling, and encourages systematic testing under varying ice growth conditions. In addition to ice growth velocity and saline water layer thickness, also sample confinement and boundary conditions are likely to be relevant (e.g., due to the processes of brine expulsion and thermal expansion). While the modelling improves on prediction of saline ice properties, micro-CT imaging will remain important in future work. E.g., the technique could be used to study the 3D evolution near the concrete-ice interface over time, and observe brine transport and crack formation in 3D and in situ (in particular at the interface, see Fig. 6). 3D microstructure data will also be valuable to set up and constrain numerical models of frost salt scaling processes (e.g., Gong and Jacobsen, 2019; Bahafid et al., 2022). Last but not least, the present results, in particular the percolation-based modelling, are relevant for the evolution of properties of young sea ice in general, considering fundamental aspects of thermal expansion and poro-elasticity (Marchenko and Lishman, 2017), strength (Anderson and Weeks, 1958; Weeks and Assur, 1964), creep (e.g., Cole, 1998; Cole, 2020) as well as permeability and fluid flow (Petrich et al., 2006; Pringle et al., 2009; Maus et al., 2021).

CRediT authorship contribution statement

Sönke Maus: Methodology, Conceptualization, Investigation, Resources, Writing-original-draft, Writing-review-editing. **Sara Bahafid:** Investigation, Conceptualization, Writing-original-draft. **Max Hendriks:** Investigation, Conceptualization, Writing-original-draft. **Stefan Jacobsen:** Conceptualization, Resources, Writing-original-draft. **Mette Rica Geiker:** Conceptualization, Funding-acquisition, Supervision, Writing-original-draft.

Declaration of Competing Interest

The authors declare that they have no known competing financial interests or personal relationships that could have appeared to influence the work reported in this paper.

Data availability

Data will be made available on request.

Acknowledgements

Appendix A. Thermodynamic properties of NaCl brine and ice

There is no international standard for the freezing point of NaCl solutions. We use the dependence of freezing point T_f on NaCl concentration S_b suggested by Maus (2007) based on the tabulated data from Zaytsev and Aseyev (1992)

$$T_f(S_b) = -0.05818 S_b (1 + 6.5067 \times 10^{-4} S_b + 5.6015 \times 10^{-6} S_b^2 - 9.2265 \times 10^{-9} S_b^3), \tag{A.1}$$

where T_f is given in °C and S_b in gram NaCl per kg solution (‰ by weight). This equation was obtained by fitting data above $S_b > 18‰$, and suffices for the non-dilute concentrations in the present work. For the brine density at its freezing point we use

$$\rho_b(T_f) = 999.843 + 0.764 S_b + 1.43 \times 10^{-4} S_b^2 + 6.82 \times 10^{-7} S_b^3. \tag{A.2}$$

from Maus (2007), given in kgm^{-3}. The ice density (also in kgm^{-3}) is approximated by the linear relationship

$$\rho_i = 916.7 (1 - 0.000164 T) \tag{A.3}$$

consistent with thermal expansion and density data of ice between 0 and -20 °C (Petrenko and Whitworth, 1999; Röttger et al., 1994). For this temperature range Eq. (A.3) implies an average thermal expansion coefficient of $\alpha_i = 5.4 \times 10^{-5}$ K^{-1}.

Appendix B. Elastic properties of NaCl brine and ice

We have estimated the temperature dependence of the brine bulk modulus K_b (inverse of the isothermal compressibility) at the freezing point of NaCl brine (and corresponding equilibrium brine salinity S_b) by extrapolating density relations for seawater (Fofonoff and Millard, 1983). Equation

$$K_b = 2.0 (1 + 0.0023 S_b) \tag{B.1}$$

approximates the brine bulk modulus K_b in GPa. For the iso-thermal bulk modulus of pure ice a constant (at -10 °C) is assumed as $K_i \approx 8.5$ GPa

(Neumeier, 2018), neglecting its temperature dependence. The elastic modulus E of pure ice is also assumed constant at $E \approx 10$ GPa. The static elastic modulus of saline ice depends on the deformation process and creep and may vary widely (Weeks, 2010). We use the equation

$$E_{si} = 10 \, exp\left(-7.1\phi_b^{1/2}\right) \tag{B.2}$$

which gives E_{si} in GPa in dependence on the fractional brine volume ϕ_b. This approximation was suggested by Sun and Scherer (2010) on the basis of several data sources. For the Poisson's ratio ν of saline ice the dependence on brine volume is neglected and a constant value of 0.33 assumed.

Appendix C. Creep stress with thermal expansion mismatch

As discussed by Valenza and Scherer (2007) the equation

$$\sigma_{ci} = \int_{T_e}^{T_f} \frac{E}{1-\nu}\left(\Delta\alpha - \frac{J_c\sigma_{ci}^3}{dT/dt}\right) dT \tag{C.1}$$

where $J_c\sigma_{ci}^3$ is the creep rate with

$$J_c = Aexp\left(-\frac{T_Q}{T + 273.15}\right) \tag{C.2}$$

describes the stress σ_{ci} in the ice that evolves due to thermal expansion mismatch $\Delta\alpha$ between ice and concrete. The equation may be solved numerically by computation of the evolving σ_{ci}, updating the ice temperature $T(n)$ and the solid fraction $\phi_s(n)$ with each temperature step ΔT, where n is the iteration number. The computational algorithm to obtain σ_{ci} may be written as (Valenza and Scherer, 2007)

$$\sigma_{ci}(n+1) = \sigma_{ci}(n)\frac{\phi_s(n)}{\phi_s(n+1)} + \Delta T \frac{E}{1-\nu}\left(\Delta\alpha - J_c(n)\sigma_{ci}^3(n)\right) \tag{C.3}$$

where the stress after the first temperature step is

$$\sigma_{ci}(0) = \Delta T \frac{E}{1-\nu}\Delta\alpha \tag{C.4}$$

Eq. (C.1) gives the evolution of the ice stress under changing temperature and solid fraction. Due to the strong dependence of creep on temperature and σ_{ci}^3, and the increasing solid fraction, we can make the assumption that the steady state solution is dominated by this final temperature. Hence we write Eq. (C.1) in the form

$$\sigma_{ci}' \approx \frac{E}{1-\nu}\left(\Delta\alpha - \frac{J_c(T_e)\sigma_{ci}^3}{dT/dt}\right)\Delta T_{fe}. \tag{C.5}$$

This neglects the nonlinear temperature dependence of J_c and the solid fraction, and approximates the solution based on J_c at the final temperature T_e, and on the temperature freezing range $\Delta T_{fe} = T_f - T_e$. This is a depressed cubic equation with the solution

$$\sigma_{ci}' = \left(\frac{C}{2} + \left(\frac{C^2}{4} + \frac{B^3}{27}\right)^{1/2}\right)^{1/3} - \left(-\frac{C}{2} + \left(\frac{C^2}{4} + \frac{B^3}{27}\right)^{1/2}\right)^{1/3} \tag{C.6}$$

wherein

$$B = \left(\frac{E}{1-\nu}\Delta T_{fe}\frac{J_c}{dT/dt}\right)^{-1}, \quad C = \frac{\Delta\alpha \, dT/dt}{Jc}$$

Hence σ_{ci}' is obtained analytically in dependence on freezing temperature T_f (and thus solute concentration), minimum temperature T_e, Elastic modulus E and the cooling rate dT/dt. Valenza and Scherer (2007) proposed parameters $A = 1.27 \times 10^{13}$ (MPa^{-3}s^{-1}) and an activation temperature $T_Q = 1.207 \times 10^4$K, based on fitting the data from Barnes et al. (1971) in the temperature range $-20 < T < -2\,°$C.[6] For the thermal expansion mismatch between pure ice and concrete, and the elastic modulus of pure ice, we use constant values for pure ice, $\Delta\alpha = 4.4 \times 10^{-5}$ and $E = 10$ Gpa. For these properties, and moderate parameter ranges ($10 < S < 90$‰, $10 < \Delta T_{fe} < 20$ K, $0.5 < dT/dt < 10$K/hour) the approximation C.6 lies within 5 % of the full numerical solution. In case of strongly varying effective α_{si} and E_{si} of saline ice the approximation gives much larger errors and should only be used with care.

---

[6] Note that $T_Q = Q/k$ with Boltzmann constant $k = 8.617 \times 10^{-5}$ eV/K where Q thus corresponds to an effective activation energy of 1.04 eV.

References

Anderson, D.L., 1960. Physical constants of sea ice. Research 13, 310–318.

Anderson, D.L., Weeks, W.F., 1958. A theoretical study of sea ice strength. Trans. Amer. Geophys. Union 39, 632–640.

Arnfeldt, H., 1943. Damage on concrete pavements by wintertime salt treatment (in swedish). Meddelande M66. Statens Väginstitut, Stockholm.

Assur, A., Weeks, W.F., 1963. Growth, structure, and strength of sea ice. Int. Assoc. Sci. Hydrol. 63, 95–108.

Bahafid, S., Hendriks, M., Jacobsen, S., Geiker, M., 2022. Revisiting concrete frost salt scaling: on the role of the frozen salt solution micro-structure. Cem. Concr. Res. 157, 106803 https://doi.org/10.1016/jcemconres.2022.106803.

Barnes, P., Tabor, D., Walker, J., 1971. The friction and creep of polychrystalline ice. Proc. Royal Soc. London, Ser. A 324, 127–155.

Bartels-Rausch, T., Jacobi, H.W., Kahan, T.F., Thomas, J.L., Thomson, E.S., Abbatt, J.P. D., Ammann, M., Blackford, J.R., Bluhm, H., Boxe, C., Domine, F., Frey, M.M., Gladich, I., Guzmán, M.I., Heger, D., Huthwelker, T., Klán, P., Kuhs, W.F., Kuo, M.H., Maus, S., Moussa, S.G., McNeill, V.F., Newberg, J.T., Pettersson, J.B.C., Roeselová, M., Sodeau, J.R., 2014. A review of air-ice chemical and physical interactions (aici): liquids, quasi-liquids, and solids in snow. Atmos. Chem. Phys. 14, 1–47. https://doi.org/10.5194/acp-14-1-2014. URL:www.atmos-chem-phys.net/14/1/2014/.

Brisard, S., Serdar, M., Monteiro, P.J., 2020. Multiscale x-ray tomography of cementitious materials: A review. Cem. Concr. Res. 128, 105824 https://doi.org/10.1016/j.cemconres.2019.105824.

Brun, M.B., Shpak, A., Jacobsen, S., 2021. Shape and size of particles scaled from concrete surfaces during salt frost testing and rapid freeze/thaw in water. Nordic Concrete Res. 64, 53–68. https://doi.org/10.2478/ncr-2021-0001.

Cnudde, V., Boone, M., 2013. High-resolution x-ray computed tomography in geosciences: a review of the current technology and applications. Earth-Sci. Rev. 123, 1–17.

Cole, D., 2020. On the physical basis for the creep of ice: The high temperature regime. J. Glaciol. 66, 401–414. https://doi.org/10.1017/jog.2020.15.

Cole, D.M., 1998. Modeling the cyclic loading response of sea ice. Int. J. Solids Struct. 35, 4067–4075.

Cox, G., 1983. Thermal expansion of saline ice. J. Glaciol. 29, 425–432.

Crabeck, O., Galley, R., Mercury, L., Delille, B., Tison, J., Rysgaard, S., 2019. Evidence of freezing pressure in sea ice discrete brine inclusions and its impact on aqueous-gaseous equilibrium. J. Geophys. Res. Oceans 124, 1660–1678. https://doi.org/10.1029/2018JC014597.

De La Chapelle, S., Milsch, H., Caselnau, O., Duval, P., 1999. Compressive creep of ice containing a liquid intergranular phase: rate-controlling processes in the dislocation creep regime. Geophys. Res. Lett. 26, 251–254.

Desrues, J., Viggiani, G., Besuelle, P., 2006. Advances in X-ray Tomography for Geomaterials. John Wiley and Sons, 2nd International Workshop on the Application of X-ray CT for Geomaterials (GeoX 2006) held in Aussois, France, on 4–7 October, 2006.

Drygalski, E., 1897. Grönlands Eis und sein Vorland. In: Grönland-Expedition der Gesellschaft für Erdkunde zu Berlin 1891–1893, vol. 1. Kühl, Berlin, pp. 555.

Duval, P., 1977. The role of the water content on the creep rate of polycrystalline ice. In: International Symposium on Isotopes and Impurities in Snow and Ice, Grenoble, Aug. 28–30, 1975, vol. 118. International Association of Hydrological Sciences, pp. 29–33.

Dykins, J.E., 1967. Tensile properties of sea ice grown in a confined system. In: Physics of Snow and ice. Hokkaido University, Sapporo, Japan, pp. 523–537.

Dykins, J.E., 1969. Tensile and flexure properties of saline ice. In: Physics of ice, 3rd International Symposium on the Physics of Ice. Plenum Press, New York, pp. 251–270.

Fagerlund, G., 1992. Effect of the freezing rate on the frost resistance of concrete. Nordic Concrete Res. 11, 20–36.

Fagerlund, G., 1993. The critical spacing factor: preliminary version. Report TVBM 7058. Division of Building Materials, LTH, Lund University.

Fofonoff, P., Millard, R.C., 1983. Algorithms for computation of fundamental properties of seawater. Unesco Tech. Pap. in Mar. Sci. 44, 53.

Gallucci, E., Scrivener, K., Groso, A., Stampanoni, M., Margaritondo, G., 2007. 3d experimental investigation of the microstructure of cement pastes using synchrotron x-ray microtomography. Cem. Concr. Res. 37, 360–368. https://doi.org/10.1016/j.cemconres.2006.10.012.

GeoDict, 2012–2022. (Geometric material models and computational preDictions of material properties,www.geodict.com).

Gong, F., Jacobsen, S., 2019. Modeling of water transport in highly saturated concrete with wet surface during freeze/thaw. Cem. Concr. Res. 115, 294–307. https://doi.org/10.1016/j.cemconres.2018.08.013.

Gopalakrishnan, K., Ceylan, H., Inanc, F., 2007. Using x-ray computed tomography to study paving materials. Proc. Inst. Civ. Eng. Constr. Mater. 160, 15–23. https://doi.org/10.1680/coma.2007.160.1.15.

Gulati, S., Hagy, H., 1982. Analysis and measurement of glue-spall stresses in glass-epoxy bonds. J. Am. Cer. Soc. 65, 1–5.

Hamberg, A., 1895. Studien über Meereis und Gletschereis (sea ice and glacier ice studies). Svenska Vetenskapsakademien, Bihang til Handlinger 21, 1–13.

Hasholt, M.T., 2014. Air void structure and frost resistance: a challenge to Powers' spacing factor. Mater. Sruct. 47, 911–923. https://doi.org/10.1617/s11527-013-0102-9.

Henkel, M., Hinrichsen, H., Lübeck, S., 2008. Non-equilibrium phase transitions. In: Absorbing phase transitions, vol. I. Springer, pp. 385.

Hinrichsen, H., 2009. Observation of directed percolation - a class of nonequilibrium phase transitions. Physics 2. https://doi.org/10.1103/Physics.2.96.

Jacobsen, S., Saether, D.H., Sellevold, E.J., 1997. Frost testing of high strength concrete: frost salt scaling at different cooling rates. Mater. Struct. 30, 33–42.

Johnson, J., Metzner, R., 1990. Thermal expansion coefficients for sea ice. J. Glaciol. 36, 343–349. https://doi.org/10.3189/002214390793701327.

Kaufmann, D.W., 1960. Sodium Chloride: The production and properties of salt and brine. Physical properties of sodium chloride in crystal, gas, and aqueous solution states. Reinhold Publishing, 587–626.

Kong, W., Wei, Y., Wang, S., Chen, J., Wang, Y., 2020. Research progress on cement-based materials by x-ray computed tomography. Int. J. Pavement Res. Technol. 13, 366–765. https://doi.org/10.1007/s42947-020-0119-8.

Kuehn, G., Schulson, E., 1994. The mechanical properties of saline ice under uniaxial compression. Ann. Glaciol. 19, 39–48.

Li, L., Aubertin, M., 2003. A general relationship between porosity and uniaxial strength of engineering materials. Can. J. Civ. Eng. 30, 644–658. https://doi.org/10.1139/L03-012.

Lieb-Lappen, R., Golden, E., Obbard, R., 2017. Metrics for interpreting the microstructure of sea ice using x-ray micro-computed tomography. Cold Reg. Sci. Technol. 138, 24–35.

Lindmark, S., 1998. Mechanisms of salt frost scaling on portland cement-bound materials: studies and hypothesis,. Phd thesis,. Lund University.

Liu, Z., Hansen, W., 2015. A hypothesis for salt frost scaling in cementitious materials. J. Adv. Concr. Technol. 13, 403–414. https://doi.org/10.3151/jact.13.403.

Lofgren, G., Weeks, W.F., 1969. Effect of growth parameters on substructure spacing in NaCl ice. J. Glaciol. 8, 153–164.

Marchenko, A., Lishman, B., 2017. The influence of closed brine pockets and permeable brine channels on the thermo-elastic properties of saline ice. Philos. Trans. Royal Soc. A 375, 20150351. https://doi.org/10.1098/rsta.2015.0351.

Maus, S., 2007. On Brine Entrapment in Sea Ice: Morphological Stability, Microstructure and Convection. Logos, Berlin, p. 538.

Maus, S., 2007. Prediction of the cellular microstructure of sea ice by morphological stability theory. Royal Society of Chemistry. Physics and Chemistry of Ice, pp. 371–382.

Maus, S., 2020. The plate spacing of sea ice. Ann. Glaciol. 61, 408–425. https://doi.org/10.1017/aog.2020.65.

Maus, S., Becker, J., Leisinger, S., Matzl, M., Schneebeli, M., Wiegmann, A., 2015. Oil saturation of the sea ice pore space. In: Proceedings - Port and Ocean Engineering under Arctic Conditions, pp. 23.

Maus, S., Leisinger, S., Matzl, M., Schneebeli, M., Wiegmann, A., 2013. Modelling oil entrapment in sea ice on the basis of microtomographic images. In: Proceedings - Port and Ocean Engineering under Arctic Conditions, pp. 22.

Maus, S., Schneebeli, M., Wiegmann, A., 2021. An x-ray micro-tomographic study of the pore space, permeability and percolation threshold of young sea ice. Cryosphere 15, 4047–4072. https://doi.org/10.5194/tc-15-4047-2021. URL:https://tc.copernicus.org/articles/15/4047/2021/.

Mellor, M., 1986. Mechanical behaviour of sea ice. In: The Geophysics of Sea Ice. Plenum Press, pp. 165–281. Ed. by N. Untersteiner.

Müller, M., Ludwig, H., Ehrhardt, D., 2019. Frost-Tausalz-Angriff auf Beton, vol. 114. Beton und Stahlbetonbau. https://doi.org/10.1002/best.201800096, pp. 392–400.

Müller, M., Ludwig, H., Hasholt, M., 2021. Salt frost attack on concrete: the combined effect of cryogenic suction and chloride binding on ice formation. Mater. Struct. 54, 189. https://doi.org/10.1617/s11527-021-01779-7.

Mullins, W.W., Sekerka, R.F., 1964. Stability of a planar interface during solidification of a dilute binary alloy. J. Appl. Phys. 35, 444–451.

Nakawo, M., Sinha, N.K., 1984. A note on brine layer spacing of first-year sea ice. Atmos.-Ocean 22, 193–206.

Neumeier, J., 2018. Elastic constants, bulk modulus, and compressibility of H2O ice Ih for the temperature range 50 k - 273 k. J. Phys. Chem. Ref. Data 47. https://doi.org/10.1063/1.5030640.

Obbard, R., Trodermann, G., Baker, I., 2009. Imaging brine and air inclusions in sea ice using micro-x-ray computed tomography. J.Glaciol. 55, 1113–1115.

Petrenko, V.F., Whitworth, R.W., 1999. Physics of Ice. Oxford University Press, p. 373.

Petrich, C., Langhorne, P.J., Sun, Z.F., 2006. Modelling the interrelationships between permeability, effective porosity and total porosity in sea ice. Cold Reg. Sci. Techn. 44, 131–144.

Pigeon, M., Marchand, J., Pleu, R., 1996. Frost resistant concrete. Constr. Build. Mater. 10, 339–348.

Pigeon, M., Prevost, J., Simard, J., 1985. Freeze-thaw durability versus freezing rate. ACI J. 61–82.

Powers, T., 1954. Void spacing as a basis for producing air-entrained concrete. J. Am. Concr. Inst. 25, 50–46.

Pringle, D.J., Miner, J.E., Eicken, H., Golden, K.M., 2009. Pore space percolation in sea ice single crystals. J. Geophys. Res. 114 https://doi.org/10.1029/2008JC005145.

Promentilla, M., Sugiyama, T., 2010. X-ray microtomography of mortars exposed to freezing-thawing action. J. Adv. Concr. Technol. 8, 97–111.

Richter-Menge, J.A., Jones, K.F., 1993. The tensile strength of first-year sea ice. J. Glaciol. 39, 609–618.

Riley, N., Noll, G., Glen, J.W., 1978. The creep of NaCl-doped ice monocrystals. J. Glaciol. 21, 501–507.

Röttger, K., Endriss, A., Ihringer, J., Doyle, S., Kuhs, W., 1994. Lattice constants and thermal expansion of H2O and D2O ice Ih between 10 and 265 k. Acta Crystall. B50, 644–648. https://doi.org/10.1107/S0108768194004933.

Sahimi, M., 1993. Flow phenomena in rocks. Rev. Mod. Phys. 65, 1393–1534.

Salomon, M., Maus, S., Pertrich, C., 2021. Microstructure evolution of young sea ice from a svalbard fjord using micro-ct analysis. J. Glaciol. 68, 571–590. https://doi.org/10.1017/jog.2021.119.

Schulson, E.M., Duval, P., 2009. Creep and fracture of ice. Cambridge University Press, p. 401.

Setzer, M., Keck, H., Palecki, S., 2007. Development of a test procedure for concrete according to XF2-exposition. Technical Report B56. Berichte der Bundesanstalt f. Strassenwesen BAST, Brücken- und Ingenieurbau.

Shokr, M., Sinha, N., 2015. Sea ice physics and remote sensing. In: Geophys. Monogr., vol. 209. John Wiley and Sons.

Shpak, A., 2020. Production and documentation of frost durable high-volume fly ash concrete: air entrainment, cracking and scaling in performance testing. Ph.D. thesis. Norwegian University of Science and Technology. Department of Structural Engineering. Doctoral theses at NTNU, 2020:366.

Sinha, N., 1986. Young arctic frazil sea ice: field and laboratory strength tests. J. Mater. Sci. 21, 1533–1546.

Stauffer, D., Aharony, A., 1992. Introduction to Percolation Theory, second ed. Taylor & Francis.

Sun, Z., Scherer, G.W., 2010. Effect of air voids on salt scaling and internal freezing. Cem. Concr. Res. 40, 260–270. https://doi.org/10.1016/j.cemconres.2009.09.027.

Sverdrup, H.U., Johnson, M.W., Fleming, R.H., 1946. The oceans - their physics, chemistry and general biology. Prentice-Hall, New York, p. 1060.

Thompson, W., 1947. The thermal conductivity of butyl rubber at low temperatures. Ph.D. thesis. The University of British Columbia.

Timco, G.W., O'Brien, S., 1994. Flexural strength equation for sea ice. Cold Reg. Sci. Technol. 22, 285–298.

Valenza, J.J., Scherer, G.W., 2006. Mechanism for salt scaling. J. Am. Ceram. Soc. 89, 1161–1179. https://doi.org/10.1111/j.1551-2916.2006.00913.x.

Valenza, J.J., Scherer, G.W., 2007. A review of salt scaling: II. mechanisms. Cem. Concr. Res. 37, 1022–1034. https://doi.org/10.1016/j.cemconres.2007.03.003.

Walker, D., 1859. Ice observations. Proc. R. Soc. London 9, 609–611.

Weeks, W.F., 1961. Studies of salt ice I: The tensile strength of NaCl Ice. CRREL Research Report 80. Cold Regions Research and Engineering Laboratory.

Weeks, W.F., 2010. On Sea Ice. University of Alaska Press.

Weeks, W.F., Assur, A., 1963. Structural control of the vertical variation of the strength of sea and salt ice. In: Kingery, W.D. (Ed.), Ice and snow. M.I.T. Press, pp. 258–276.

Weeks, W.F., Assur, A., 1964. Structural control of the vertical variation of the strength of sea and salt ice. CRREL Research Report 113. Cold Regions Research and Engineering Laboratory.

Yener, E., 2015. A new frost salt scaling mechanism for concrete pavements based on brine rejection from ice layer adhered to concrete surface. Road Mater. Pavement Des. 16, 89–100. https://doi.org/10.1080/14680629.2014.975153.

Zaytsev, I.D., Aseyev, G.G., 1992. Properties of aqueous solutions of electrolytes. CRC Press, Boca Raton, p. 1773.

Zehfuss, J., Robert, F., Spille, J., Razafinjato, R.N., 2020. Evaluation of eurocode 2 approaches for thermal conductivity of concrete in case of fire. Civil Eng. Des. 2, 58–71. https://doi.org/10.1002/cend.202000001.

Zhang, M., Jivkov, A.P., 2014. Microstructure-informed modelling of damage evolution in cement paste. Constr. Build. Mater. 66, 731–742. https://doi.org/10.1016/j.conbuildmat.2014.06.017.